PCCP

PAPER

View Article Online
View Journal | View Issue

Cite this: *Phys. Chem. Chem. Phys.*, 2015, **17**, 20941

A detailed study of cholinium chloride and levulinic acid deep eutectic solvent system for CO_2 capture *via* experimental and molecular simulation approaches†

Ruh Ullah,[a] Mert Atilhan,*[a] Baraa Anaya,[a] Majeda Khraisheh,[a] Gregorio García,[b] Ahmed ElKhattat,[a] Mohammad Tariq[a] and Santiago Aparicio*[b]

Received 10th June 2015,
Accepted 29th June 2015

DOI: 10.1039/c5cp03364k

www.rsc.org/pccp

Choline chloride + levulinic acid deep eutectic solvent is studied as a suitable material for CO_2 capturing purposes. The most relevant physicochemical properties of this solvent are reported together with the CO_2 solubility as a function of temperature. The corrosivity of this solvent is studied showing better performance than amine-based solvents. A theoretical study using both density functional theory and molecular dynamics approaches is carried out to analyze the properties of this fluid from the nanoscopic viewpoint, and their relationship with the macroscopic behavior of the system and its ability for CO_2 capturing. The behavior of the liquid–gas interface is also studied and its role on the CO_2 absorption mechanism is analyzed. The reported combined experimental and theoretical approach leads to a complete picture of the behavior of this new sorbent with regard to CO_2, which together with its low cost, and the suitable environmental and toxicological properties of this solvent, lead to a promising candidate for CO_2 capturing technological applications.

1. Introduction

Carbon dioxide capture is one of the most relevant technological,[1] environmental,[2] social[3] and economic[4] needs nowadays. The effect of anthropogenic CO_2 atmospheric emissions on global warming has been widely proven,[5,6] which in all the considered scenarios will lead to increasing temperatures at a global level,[7] with large economic, social and environmental consequences.[8,9] The most important source of anthropogenic CO_2 emissions rises from the combustion of fossil fuels for transportation, power generation and industrial purposes.[10–12] In particular, electricity production from fossil fuelled power plants is responsible for a large percentage of total anthropogenic CO_2 emissions,[13,14] and thus, reducing these emissions has a pivotal role for controlling climate change. In spite of the remarkable advances in renewable electricity production approaches, the state-of-the-art of these methods is not an alternative to fossil fuels, and thus, all the projections show that power plants based on fossil fuels will develop a pivotal role for energy production in the coming decades.[15,16] Therefore, a realistic approach for reducing CO_2 emissions in a reasonable time frame is to develop suitable technologies that allow for the capturing of CO_2 from flue gases in fossil fuelled power plants.[17–22]

The state-of-the-art of CO_2 capture technologies does not allow carbon capture without an unacceptable increase in the costs of electricity generation,[23–25] which hinders their application for the required large scale. The most common approach for carbon capture is post-combustion sorption based on alkanolamine liquid sorbents,[26,27] which although showing large affinity for CO_2 molecules has serious technological drawbacks, such as facilitating corrosion, solvent evaporation or degradation, and large capturing costs.[23,28–35] Therefore, alternative CO_2 sorbents have been studied in the last few years such as metal–organic frameworks,[36] solid sorbents,[37] carbon-based materials,[38] or membranes.[39] One alternative that has attracted great attention are ionic liquids, IL,[40–42] because of the possibility of tuning their properties, and thus their affinity for CO_2 molecules, through the selection of suitable ions. Nevertheless, ILs have also showed some problems with regard to their application for carbon capture purposes, such as their high viscosity or their cost, which have hindered their application for capturing purposes at the industrial scale.[43–48] Therefore, although these drawbacks should not be considered as a motive for discarding ILs as possible CO_2 capturing candidates,[49–52] several alternatives have been proposed

---

[a] *Department of Chemical Engineering, Qatar University, P.O. Box 2713, Doha, Qatar. E-mail: mert.atilhan@qu.edu.qa*

[b] *Department of Chemistry, University of Burgos, 09001 Burgos, Spain. E-mail: sapar@ubu.es*

† Electronic supplementary information (ESI) available: Table S1 (forcefield parameterization), Table S3 (physicochemical properties), Table S4 (NMR data) and Fig. S1 (*in situ* FTIR apparatus setup), Fig. S2 (sorption apparatus setup) and Fig. S3 (*in situ* FTIR data). See DOI: 10.1039/c5cp03364k

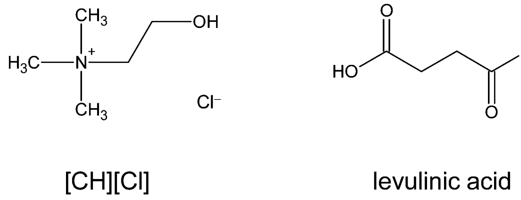

Fig. 1 Molecular structure of [CH][Cl] salt and levulinic acid.

to maintain the design flexibility of ILs while avoiding their well-known problems. Deep eutectic solvents (DES) are among the most promising options to overcome these IL problems while retaining their positive properties and the ability of tuning their behavior.[53,54] DESs are usually a binary mixture of a salt (or IL) with an hydrogen bond donor (HBD), which at a certain molar ratio leads to a system with a melting point close to ambient temperature and lower than those for the pure compounds of which the DES is comprised.[53,54] Although several salts have been proposed for developing DESs, most of the available literature is based on cholinium chloride ([CH][Cl]) (Fig. 1).[54] [CH][Cl] is a non-toxic and biodegradable compound, and it can be obtained at very low cost.[55,56] [CH][Cl] may lead to a DES when mixed with different types of HBDs such as urea, polyols (glycerol or ethylene glycol), sugars or carboxylic acids. To maintain the suitable characteristics of [CH][Cl] when developing DESs, this salt has to be combined with suitable HBDs, and thus, an approach is vary the HBDs used.[57,58] In recent works Maugeri *et al.*[59] and Florindo *et al.*[60] proposed the use of HBDs combined with [CH][Cl]. Levulinic acid ([LEV]) is a compound which is fully biodegradable and non-toxic, that may be obtained from biomass at low costs,[61–63] and thus [CH][Cl] + [LEV] DES (Fig. 1) may be considered as a renewable material. [CH][Cl] + [LEV] lead to a DES when mixed ([CH][Cl]:[LEV] at a 1:2 molar ratio, CHCl_LEV_1_2).[59,60] The available studies on CO_2 capture using [CH][Cl] based DESs are mostly limited to systems containing HBDs such as urea, glycerol, ethyleneglycol, or carboxylic acids such as malonic or lactic,[64–72] but no studies for DES involving [LEV] are reported. Therefore, a study on the suitability of CHCl_LEV_1_2 DES for CO_2 capturing purposes is reported in this work. Considering that a full characterization of this material is required in order to analyze its weaknesses and strengths for carbon capture purposes, a physicochemical characterization of CHCl_LEV_1_2 was carried out, in which the most remarkable properties were selected, both because they are required for process design purposes and/or because they provide information about the structure and behavior of the fluid. CO_2 absorption was studied at isothermal conditions at pressures up to 30 bar. Likewise, in order to understand the mechanism of CO_2 absorption at a nanoscopic level, a theoretical study using both molecular dynamics (MD) and quantum chemistry — in the density functional theory (DFT) framework — approaches was reported. The fluid's structure was studied for pure CHCl_LEV_1_2 and for the same fluid after CO_2 absorption as a function of temperature, pressure and amount of absorbed CO_2 *via* MD simulations. Short-range interactions in the fluid were analyzed in detail from DFT calculations. Likewise, considering the relevance of liquid–gas interfacial behavior for CO_2 capturing purposes, MD simulations were also carried out to analyze the behavior of CO_2 molecules at the DES surface. The reported study shows for the first time a combined full experimental and computational characterization of DESs as sorbents for CO_2 capturing purposes.

2. Methods

2.1 Materials

Levulinic acid (CAS: 123762, Aldrich) and choline chloride (CAS: 67481, Iolitec) were used as received. A mixture of 1:2 molar ratio of [CH][Cl]:[LEV] acid (CH_Cl_LEV_1_2 DES) was prepared by mixing 46.54 g of chlorine chloride and 77.41 g of [LEV]. The resulting mixture was stirred for 2 hours using a magnetic stirrer. The formation of a eutectic solution was examined and confirmed using both NMR (Varian Unity Inova 400 MHz) and FTIR spectrometry (Spectrum 400, PerkinElmer, USA). CH_Cl_LEV_1_2 DES samples were prepared by mixing the ionic liquid and acid at room temperature in a glove box compartment. Water content (1.69 wt%) was measured using Karl Fischer coulometric titration (Metrohm 831 KF coulometer) to 0.3% accuracy in water mass content.

2.2 Experimental details

NMR measurements were performed using a Varian Unity Inova 400 MHz instrument at 298.15 K (±0.1 K) for the ^1H and ^{13}C nuclei. CHCl_LEV_1_2 samples were prepared in 5 mm NMR tubes, with 0.005 g of CHCl_LEV_1_2 mixed with 1 mL of D_2O.

The formation of DES was examined and confirmed using a FTIR spectrometer (Spectrum 400, PerkinElmer, USA). Other than the FTIR studies for the characterization of the DES system, *in situ* FTIR measurements were carried out using a Bruker® Vertex 80 Fourier transform infrared spectrometer, which was coupled with a temperature controlled high pressure liquid cell (HPL-TC) that can accommodate pressures of up to 30 bar, supplied by Harrick™ Scientific. HPL-TC was equipped with high-resolution Si windows, teflon spacers of 2280 micron path-length and Viton® O-rings. The path-length was intentionally kept long to provide more volume, and therefore increase the contact opportunity with CO_2. In order to adjust CO_2 pressure, a gas feeding manifold system was designed and the schematics are shown in Fig. S1 (ESI†).

Density and viscosity were both measured using Anton Paar DMA 4500M and Lovis 200 M/ME units respectively. The density meter uses the oscillating U-tube sensor principle and it has a volume requirement of 1 mL of sample. The density meter has a reported accuracy of 0.00005 g m^{-3} in density and ±0.05 K in temperature. The Anton Paar Lovis 200 rolling ball viscometer measures the rolling time of a ball through transparent and opaque liquids according to Hoeppler's falling ball principle with ±3% viscosity uncertainty and ±0.02 K accuracy in temperature measurements.

The pH and conductivity measurements were performed at 293.15 K using a pH/conductivity meter (3200M Multiparameter Analyzer, Agilent Technologies, USA). The conductivity and the pH of the final product was 752.85 ± 5.2 μs cm^{-1}

and 2.7 ± 0.2, respectively, at a temperature of 293.15 K. Indeed, conductivity is an important indicating property, determining if an IL can play the role of both the solvent and the electrolyte in electrochemical reactions. Ionic liquids exhibit a broad range of conductivities from 0.1 to 20 mS cm^{-1} as conductivity is affected by many factors such as density, viscosity, anionic charge, ion size, delocalization, aggregation and ionic motion.[73] Recently, some DES liquid systems based on choline chloride,[74] with properties similar to those of ionic liquids, have been prepared by mechanically mixing two different components, where choline can be used as an alternative cation in combination with a suitable anion to generate ionic liquids.

Refractive indices were measured relative to the sodium D-line ($\pm 1 \times 10^{-5}$) using an automated Leica AR600 refractometer, with the sample temperature being controlled using a Julabo F25 external circulator and measured with a built-in thermometer (±0.01 K). A standard supplied by the manufacturer was used for refractometer calibration.

Corrosion experiments were conducted using circular specimens of carbon steel 1018 (0.186 wt% C, 0.214 wt% Si, 0.418 wt% Mn, 0.029 wt% P, 0.019 wt% S, balance Fe) with 1.93 cm^2 surface area of specimen exposed to the medium. Carbon steel 1018 is selected for corrosion experiments since it is a common material that is used in process equipment in chemical industries. The specimens were prepared according to ASTM G1-03 standard by wet grinding and polishing using 320 600 and 1200 grit SiC papers. The specimen was then degreased by high purity acetone, rinsed with deionized water and dried with hot dry air.[75] Electrochemical experiments were conducted in a 100 cm^3 jacketed micro cell supplied by Autolab (Fig. 2). The microcell was equipped with a potentiostat (Autolab PGSTAT101) and data acquisition system (NOVEA 1.7). The corrosion cell consisted of an Ag/AgCl reference electrode filled with 3 M KCl solution, two 316 stainless steel counter electrodes and the working electrode. A heated water circulator was connected to the outer cell jacket throughout experiments for temperature control. A water-cooled condenser was utilized to minimize vaporization losses of the test solution. Gas supply streams and a CO_2 gas flow meter was connected to the cell. Throughout all experiments, a gas stream was maintained in the gas phase of the cell. Open circuit potential OCP measurement of the specimen against the reference electrode was recorded until it was stable (defined as ±0.01 mV between successive readings). The polarization curve was generated directly by the data acquisition system in the range of ±250 mV *vs.* OCP and a scan rate of 0.001 V s^{-1}. Tafel extrapolation method was used to determine the corrosion current (I_{corr}) which was converted to corrosion rate by the following equation:

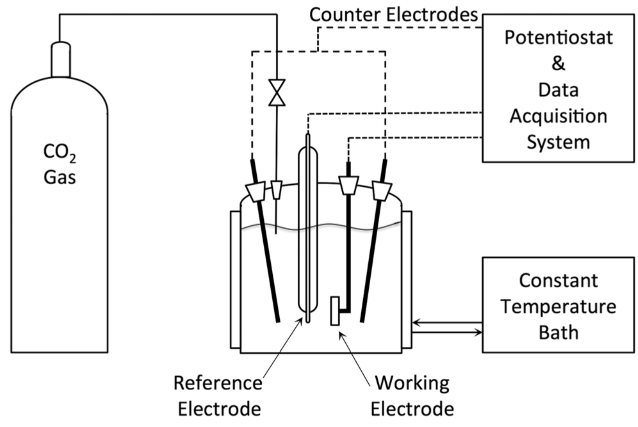

Fig. 2 Experimental set-up for electrochemical corrosion tests.

$$\mathrm{CR} = \frac{3.27 \times 10^{-3} \times I_{\mathrm{corr}} \times \mathrm{EW}}{\rho} \quad (1)$$

where CR is corrosion rate in (mm $year^{-1}$), I_{corr} is corrosion current in (μA cm^{-2}), EW is the equivalent weight of the carbon steel specimen (g per equivalent) and ρ is the density of the specimen (g cm^{-3}). The numerical value that appears in eqn (1) is a constant that defines the units for the corrosion rate and it is calculated from the calibration of the apparatus.

Thermal stability analysis of materials was performed with a Perkin Elmer Pyris 6 TGA instrument, where samples were heated in a N_2 environment from 303 K to 873 K at the rate of 5 min^{-1}.

For carbon dioxide adsorption measurements, a high-pressure magnetic suspension sorption apparatus (MSA) made by Rubotherm Präzisionsmesstechnik GmbH was used. A schematic of the apparatus is given in Fig. S2 (ESI†). The MSA apparatus is rated up to 350 bar at 373 K. The MSA has two different operation positions. First, the measurement cell is filled with CO_2 gas, and the MSA records the weight change of the sample that is placed in the sample container as the high-pressure gas is absorbed by the sample. The second measurement position is used to measure the *in situ* density of the high-pressure gas, which is required to calculate the amount of the gas adsorbed onto the sample in the high-pressure cell. In this work, pressures of up to 30 bar were used as the maximum pressure, and at the end of each isotherm, a hysteresis check was conducted for each isotherm by collecting desorption data as the system was depressurized. The nature of physical adsorption was later cross-checked by comparing before and after FTIR measurements of the DES sorbent. CO_2 adsorption–desorption isotherms were selected at 298.15 K and 323.15 K. Detailed operating principles and data correlation of the magnetic suspension force transmission is also discussed previously elsewhere.[76,77]

For buoyancy calculations used in sorption measurements, the *in situ* density of the pressurized gas in the high-pressure cell was measured. Archimedes' principle was used for density measurements by utilizing a calibrated silicon sinker placed just above the sample basket in the pressure cell. The silicon sinker used in this apparatus had a volume of 4.4474 cm^3 measured at 20 °C with a 0.0015 cm^3 uncertainty and a density of 4508 kg m^{-3} measured at 293.15 K with a 4 kg m^{-3} uncertainty. On the other hand, the uncertainty for pressure measurements was ±0.05% in the full scale of the 350 bar rated pressure transducer and ±0.1 K for the temperature measurements.

2.3 Simulations

Optimizations were performed from those systems composed of one isolated molecule (*i.e.* ions, levulinic acid or CO_2) up to systems composed of DES and CO_2 (CHCl_LEV_1_2$\cdots$$CO_2$). Optimized minima were checked trough their vibrational frequencies. For those simulations wherein two or more molecules are present, different starting points were employed in order to study different relative dispositions, focusing our attention on the disposition of minimal energy. All these calculations were carried out using B3LYP[78,79] coupled with dispersion corrections according to Grimme's scheme[80] (B3LYP-D2), with the 6-31+G** basis set. B3LYP was selected since it has showed a remarkable performance over a wide range of systems,[81] while dispersion corrections are adequate since we are considering systems with dispersive interactions such as hydrogen bonds.[80] Besides, calculated energies after dispersion corrections are comparable with more reliable values, such as those obtained at the MP2 level.[82]

From those systems composed of two or more molecules, computed energies were corrected (to avoid basis set superposition error) according to counterpoise procedure.[83] Interaction energies (ΔE) for different processes related to CO_2 capture and formation of DES were computed. Thus, ΔE for CHCl_LEV_1_2$\cdots$$CO_2$ (*i.e.* CO_2 capture using DES) was calculated as: $\Delta E_{\text{DES–CO}_2} = E_{\text{DES–CO}_2} - (E_{\text{DES}} + E_{\text{CO}_2})$, $E_{\text{DES–CO}_2}$, E_{DES} and E_{CO_2} being the (counterpoise corrected) energies for CHCl_LEV_1_2$\cdots$$CO_2$, CHCl_LEV_1_2 and CO_2, respectively. Intermolecular interactions were analyzed by means of Atoms in Molecules (AIM) theory.[84] Topological analyses according to AIM theory were carried out using the MultiWFN package.[85] According to Bader's theory,[84] there are four kinds of critical points, but given the characteristics of the studied systems and to improve and clarify data analysis we have mainly focused over bond critical points (BCP), which raises the criteria for considering the presence of intermolecular interactions. Finally, atomic charges were computed to fit the electrostatic potential according to the ChelpG scheme.[86] All calculations were carried out with Gaussian 09 (Revision D.01) package.[87]

MD simulations were carried both for pure CHCl_LEV_1_2 and for CHCl_LEV_1_2 + CO_2 systems. In the case of pure DES, 250 [CH][Cl] ion pairs plus 500 [LEV] molecules were considered for all the simulations in the 298 to 348 K temperature range at 0.1 MPa of pressure. Mixed CHCl_LEV_1_2 + CO_2 were prepared according to the experimental solubility data obtained in this work, and thus, four different mixed systems were prepared for simulations at 298 K, all of them containing the same number of ion pairs and [LEV] molecules as for pure DES simulations and with a different number of CO_2 molecules to mimic experimental adsorption isotherms up to 1 MPa (samples CHCl_LEV_1_2_CO_2_I, CHCl_LEV_1_2_CO_2_II, CHCl_LEV_1_2_CO_2_III, and CHCl_LEV_1_2_CO_2_IV; Table S2, ESI†). All these simulations were carried out in the *NPT* ensemble, with initial low density boxes ($\sim$0.2 g cm^{-3}) built using the Packmol program.[88] Simulations were carried out starting from these initial boxes being equilibrated during 5 ns with additional 10 ns runs collected for production purposes.

In the case of MD simulation for the analysis of interfacial behavior, a box of CHCl_LEV_1_2 with the same characteristics of those used for the simulation of pure DES, and previously equilibrated, was put in contact along the *z*-direction with (i) a vacuum layer (with the vacuum layer dimension in the *z*-coordinate three-times larger than the DES layer) for describing the DES–vacuum interface, and (ii) with a CO_2 gas phase (with gas layer also being three-times larger in the *z*-dimension than the DES liquid layer) for considering the DES–CO_2 gas interface. The density of the CO_2 gas layer corresponded to that at 298.15 K and 10 bar obtained from CO_2 reference equations of state.[89] These interfacial simulations were carried out in the *NVT* ensemble at 298.15 K.

All the MD simulations were carried out using the MDynaMix v.5.2 molecular modeling package.[90] Pressure and temperature were controlled using the Nosé–Hoover thermostat. Coulombic interactions were handled with the Ewald summation method,[91] with cut-off radius of 15 Å. A Tuckerman–Berne double time step algorithm,[92] with long and short time steps of 1 and 0.1 fs, was considered for solving the equations of motion. Lorentz–Berthelot mixing rules were used for Lennard-Jones terms.

The forcefield parameterization used along MD simulations is reported in Table S1 (ESI†). This parameterization was developed using DFT calculations for clusters formed by 1[CH][Cl] + 2[LEV] molecules which were optimized as reported in the previous section, and thus, ChelpG[86] charges were calculated for this cluster. The optimized structures for this model cluster show that LEV molecules may interact in two different positions (see Results and discussion section), with [LEV] molecules having different charges depending on the interacting site. Therefore, the parameterization used considers two types of levulinic acid molecules (LEV_I and LEV_II) with different charge parameters (Table S1, ESI†). The proposed parameterization leads to charges of +0.8254 for $[CH]^+$, −0.6849 for Cl^-, −0.0663 for LEV_I, and −0.0743 for LEV_II. This parameterization was developed to obtain a more realistic physical picture of the charge distribution in the studied DES instead of applying the simplified option of ±1 total charge for the cation/anion and null charges for any LEV molecule.

3. Results and discussion

3.1 Density, refraction index and viscosity

These properties were collected (Table S3, ESI†) and are presented in Fig. 3. Similar DES systems have been studied and their density and viscosity profiles have been reported elsewhere for CHCl and levulinic acid,[60] glyceric acid,[60] phenol,[93] urea,[94] and glycerol[95] containing DES systems. Density and viscosity values are important for these exotic mixtures for the development of suitable equations of state, which has a crucial role in the calculation of further thermodynamic properties for developing industrial processes including gas separation operations that run with novel solvent substitutes for amines. Most of the studied DES system densities are in the range of 1–1.35 g cm^{-3} at 25 °C. DES systems that contain metallic salts show a tendency to have higher

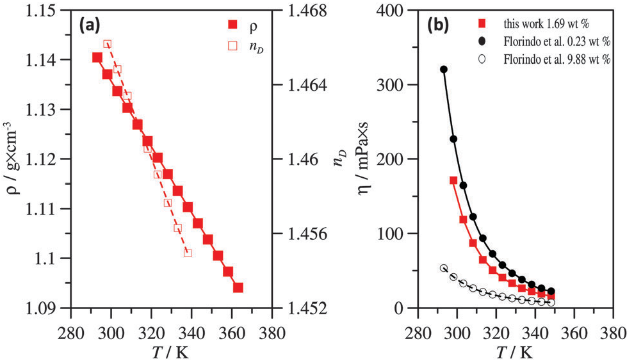

Fig. 3 Experimental (a) density, ρ, refraction index, n_D, and (b) viscosity, η, data for CHCL_LEV_1_2 DES system. In panel (b), a comparison of η data with those reported by Florindo *et al.*[60] is reported considering the water content (wt%) of used samples. Error bars are not reported because they are smaller than point size.

densities at room temperature in the range of 1.3–1.6 g cm^{-3}. [CH][Cl] and urea DES systems (with 1 : 2 ratio) have been reported to have 1.25 g cm^{-3} density at 293.15 K.[96] For the experimented CHCl_LEV_1_2 DES system, density values fall in the range of 1.14–1.10 g cm^{-3} within the temperature range of 293.15–363.15 K. This shows a similarity of the values of a similar DES system formed with [CH][Cl] and a different acid based HBD. Refractive indices follow a linear trend in the 298.15 K to 238.15 K range with values of 1.466–1.455. These refractive index values are in the lower range for the DESs studied in the literature, nevertheless they show that CHCl_LEV_1_2 DES is a highly polarizable solvent.[96]

On the other hand, viscosity has also been extensively measured for the available DESs, due to its importance for industrial purposes. Viscosity data are required for DES applications not only in gas solubility and separation processes but also fields such as lubrication or any other potential high-pressure operation have been considered as well.[97] Moreover, viscosity data is essential to realize the possible mass transfer coefficient limitations as well as fluid pumping issues for advanced process system and equipment design purposes. The [CH][Cl] couple with various HBD DES systems have recently been investigated and their viscosities have been reported and quite high viscosity values have been observed. For the [CH][Cl] and urea 1 : 2 DES system, a viscosity of 750 mPa s at 298.15 K has been reported.[94] Moreover, for [CH][Cl] and glycerol,[95] ethylene glycol,[94] glycolic acid,[60] and phenol[93] DES systems, viscosity values of 246.8, 35, 394.8 and 35.1 mPa s at 303.15 K have been observed, respectively. For the experimented CHCl_LEV_1_2 DES system, a viscosity of 171.3 mPa s at 298.15 K has been observed in this work. Florindo *et al.*[60] also reported a viscosity value of the same system for temperatures between 298.15 K and 350 K (*e.g.* 226.8 mPa s at 298.15 K). The difference between the viscosity data reported in this work and those by Florindo *et al.*[60] rises from (i) the different methodology for sample preparation (grinding of the DES components by Florindo *et al.*,[60] *cf.* mixing in this work), and (ii) the different water content. The most remarkable feature should be the water content, which develops a pivotal role for viscosity measurements. The sample used in this work has a water content of 1.6 wt% which is higher than the 0.23 wt% of the sample used by Florindo *et al.*,[60] which would justify the lower viscosity data reported in this work (Fig. 3b). This is confirmed by the viscosity data reported by Florindo *et al.*[60] for CHCl_LEV_1_2 DES saturated with water (9.88 wt%), which shows less viscous behavior than the sample used in this work.

3.2 NMR and FTIR

^{1}H and ^{13}C NMR features are summarized in Table S4 (ESI†), the data are in good agreement with those by Florindo *et al.*[60] and it discards the presence of relevant impurities at least at the NMR detection levels. FTIR characterization of the DES structure provides information about interactions and complexation between constituents. FTIR spectra of pure [LEV] and choline chloride are given in Fig. S1 (ESI†). Regarding pure [LEV], vibrational bands at 1720–1695 cm^{-1}, 1435–1400 cm^{-1}, 1380–1345 cm^{-1} and 1225–1100 cm^{-1} refer to the presence of aliphatic ketone, while the vibrational bands at 1720–1701 cm^{-1} refer to a carbonyl compound. The FTIR spectrum of the [LEV] confirms its classification as a keto-acid. For pure choline chloride, vibrational bands at 3540–3200 cm^{-1} and 1205–885 cm^{-1} refer to the presence of a hydroxyl or amino group, while those bands at 2990–2855 cm^{-1} and 1485–1415 cm^{-1} refer to the presence of an alkyl group. On the other hand, the formation of DES was confirmed by the FTIR spectrum of CHCl_LEV_1_2 DES 1 : 2 molar ratio as shown in Fig. 4, where, the vibrational bands at 2990–2855 cm^{-1} and 1485–1415 cm^{-1} indicate the presence of an alkyl group, the bands at 1720–1695 cm^{-1}, 1435–1400 cm^{-1}, 1380–1345 cm^{-1} and 1225–1100 cm^{-1} represent the aliphatic ketone group, 1720–1701 cm^{-1} bands refer to a carbonyl compound, and 1745–1710 and 1300–1000 cm^{-1} bands refer to an ester or ketone compound.

3.3 *In situ* FTIR

For *in situ* FT-IR measurements, a temperature controlled high-pressure liquid cell (HPL-TC) manufactured by Harrick Scientific was used. HPL-TC was equipped with specific internal parts: high-resolution Si windows, Teflon™ spacers of 2280-micron path-length and Viton O-rings. The path-length was intentionally kept thick to provide more volume, and therefore increase the contact opportunity between CO_2 and the solvent molecules as well as to provide a more stable sealed system. In order to manipulate CO_2 injection at the desired pressures under isothermal conditions, a particular system was designed and attached to the spectrometer. *In situ* FTIR experiments were performed at 50 °C over a range of low CO_2 pressures. To ensure thermal stability, the thermo-regulator was kept operating for at least one hour prior to the experiment. A background spectrum of the HPL-TC system under vacuum was collected before and after each DES *in situ* FTIR measurement and this background was subtracted from the DES + CO_2 spectrum data. To this end, the sample spectrum was collected upon exposure to CO_2. This sample spectrum is believed to be influenced by

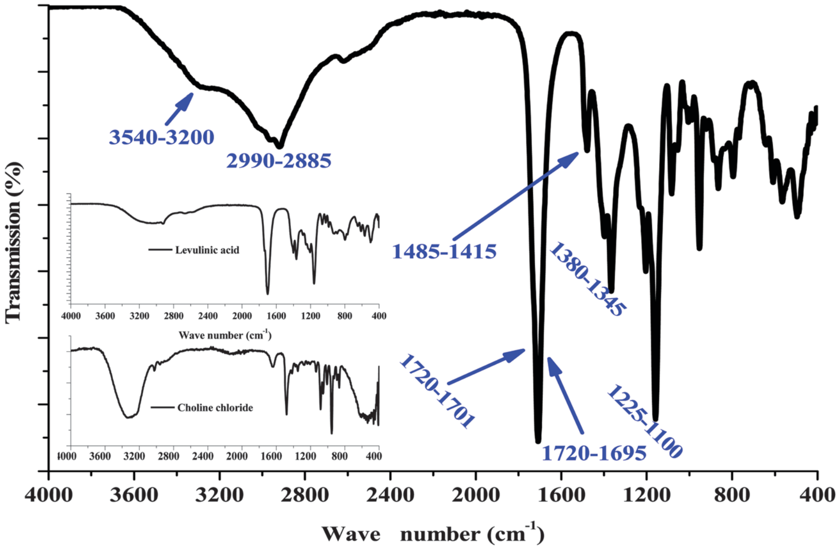

Fig. 4 FTIR characterization results for [CH][Cl], [LEV] and CHCL_LEV_1_2 DES system.

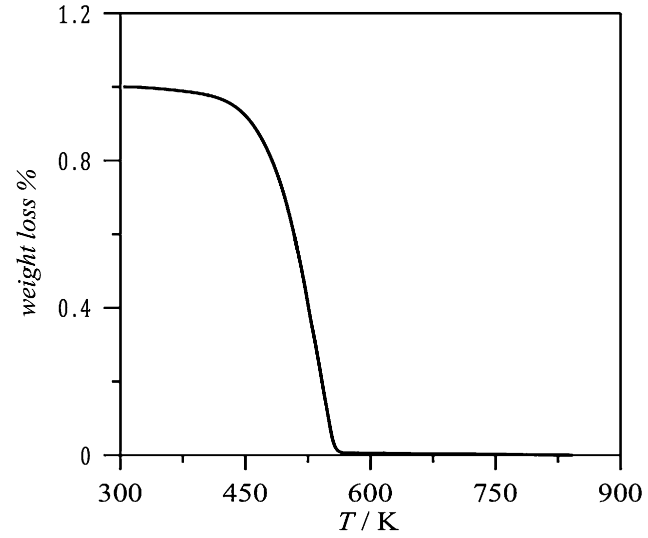

Fig. 5 Thermal gravimetric analysis of CHCL_LEV_1_2 DES system.

the contribution of both CO_2 in the absorbed phase (dissolved in DES) and gaseous CO_2 in the bulk especially as the path-length is thick. Hence, in order to eliminate the gaseous CO_2 contribution, pure CO_2 spectra were collected separately at the same conditions of the sample spectrum, and then each was subtracted from the sample spectrum that corresponds to same operating conditions. *In situ* FTIR experimental findings of CHCL_LEV_1_2 DES with the presence of pressurized CO_2 at different pressures are shown in Fig. S3 (ESI†). Near the CO_2 fundamental bending mode (600–700 cm^{-1}), interesting gradual bands appear around 619 cm^{-1} analogous to the red-shifted bending mode band observed in the computational results which was overlapping with other CO_2-free DES and CO_2-loaded DES bands. The subtraction of gaseous CO_2 and DES spectra resulted in a loss of CO_2 related bands that are overlapped and appeared as negative split bands. Nevertheless, the effect of the increasing pressure was observed and recognized by the increase in intensity that corresponds to the increase in the concentration of absorbed CO_2 in the liquid DES phase.

3.4 TGA

Thermal gravimetric analysis (TGA) of the DES system was performed to investigate the temperature limitation of the absorbent. Fig. 5 shows the TGA profile of the experimented DES system. Single step degradation behavior was observed and the analysis shows that the DES system is stable up to 453–473 °C, which makes the experimented DES system suitable for high temperature post combustion CO_2 capture process conditions as well.

3.5 Corrosion measurements

Needless to say that corrosivity is one of the most important concerns from a process operation point of view. It is necessary both to forecast the equipment depreciation with time, and also to make plans not only during material selection for equipment design, but also during operation by selection of appropriate corrosion inhibitors to prevent potential corrosion within the pipe and absorption column vessel. For this purpose, corrosion experiments have been conducted for the DES system and monoethanolamine (MEA) system, as it is the most widely used CO_2 capture agent currently used in chemical plants. Fig. 6 shows the current density *vs.* potential plot for the two studied DES and MEA systems. The details on how to interpret the polarization curve are given in Section 2.2 of this work. Two identical carbon steel samples were used for the corrosion experiments and they were prepared for the measurements as per ASTM G1-03 standards as mentioned in above section. The surface area of the specimens was calculated to be 1.93 cm^2. The analysis on the polarization curves for the CO_2 loaded DES system showed that the corrosion potential is −0.43 V and the corresponding corrosion rate behavior is 0.027 mm $year^{-1}$. On the other hand, the corrosion behavior of the identical carbon

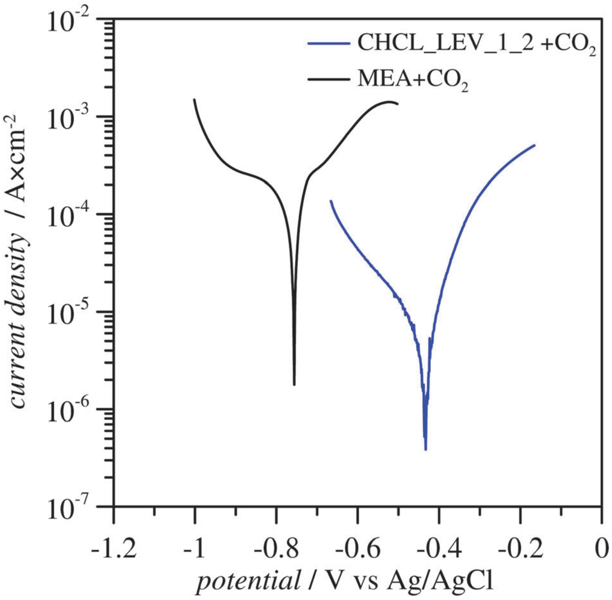

Fig. 6 Corrosion resistance performance experiments for CO_2 saturated CHCL_LEV_1_2 DES system and its comparison with CO_2 saturated MEA system.

steel specimen in the CO_2 loaded MEA solution was also conducted. The corrosion potential was recorded to be −0.75 V and the corresponding corrosion rate was calculated to be 0.54 mm year^{-1}. These results show that from a corrosion point of view, the DES system exhibits much more corrosion resistant behavior when compared with the MEA system, and this considerable order of magnitude difference is a great advantage in reducing the both operating and fixed cost of the absorber column and its ancillary equipment in a CO_2 capture plant.

3.6 CO_2 solubility

CO_2 solubility studies were conducted by using state of the art magnetic suspension based MSA and the details of the apparatus are mentioned in the experimental section. Pressure transducers (Paroscientific, US) were used in a range from vacuum up to 35 MPa with an accuracy of 0.01% in full scale. The temperature was kept constant with an accuracy of ±0.5 K for each measurement (Minco PRT, US). *In situ* density values for CO_2 were measured during sorption measurements as it is necessary to calculate the absorbed amount of CO_2, and density values were cross-checked with REFPROP 9.0[98] for consistency purposes. Absorption measurements were carried out using 2 to 3 mL DES samples. First the system was placed under vacuum for 8 hours at 293 K, 298 K, 308 K, 318 K and 323 K. CO_2 was then pressurized through a Teledyne Isco 260D fully automated compressor and fed into the high-pressure measurement cell in which the CO_2 absorption process begun. Once the solubility equilibrium was reached, measurements were taken for a period of 10 minutes; each data point was collected at 30 second time intervals. At the end of each measured pressure point, a gas-dosing system triggered the compressor to the next pressure measurement point, which increased the measurement cell pressure in a step-wise manner. In this work, pressure up to 3 MPa (30 bars) was used for the maximum pressure and 293 K, 298 K, 308 K, 318 K and 323 K isotherms were investigated for CO_2 absorption in the DES system. A solubility hysteresis check was conducted at each isotherm by collecting desorption data as the system was depressurized. Details of the solubility experiment were based on the amount of absorbed carbon dioxide in the sample as calculated by using the below equation:

$$W + W_{\text{buoy,sample}} + W_{\text{buoy,sink}} = m_{\text{abs}} + m_{\text{sample}} + m_{\text{sink}} \quad (2)$$

where W = signal read by the instrument; $W_{\text{buoy,sample}} = V_{\text{sample}} \times d_{\text{gas}}$ = buoyancy correction due to sample; V_{sample} = volume of the sample; d_{gas} = density of the gas; $W_{\text{buoy,sink}} = V_{\text{sinker}} \times d_{\text{gas}}$ = buoyancy correction due to sinker; V_{sinker} = volume of the sinker; m_{abs} = absorption amount; m_{sample} = mass of the sample; m_{sink} = mass of the sinker (sinker is a float that is used for *in situ* gas density measurements).

Fig. 7 shows the findings of the solubility measurements at 5 different isotherms up to a pressure of 30 bar. It was observed that the maximum amount of CO_2 solubility was decreased with an increase in temperature. The DES system absorbed 2.316, 2.220, 2.100, 2.027 and 1.934 mmol of CO_2 per gram of DES sample at 293 K, 298 K, 308 K, 318 K and 323 K, respectively, at the maximum operating pressure of 30 bar. The direct weight measurement technique allows *in situ* observation of the behavior of the measured sample. In other words, a potential swelling effect can be observed during the measurements. In the case of swelling of the sample, the increased sample volume would cause an increase in the buoyancy on the measurement cell, which in turn would give the impression of a decrease in the amount of captured CO_2. However, it can be seen from Fig. 7 that the CO_2 absorption trend has been reported as a curve

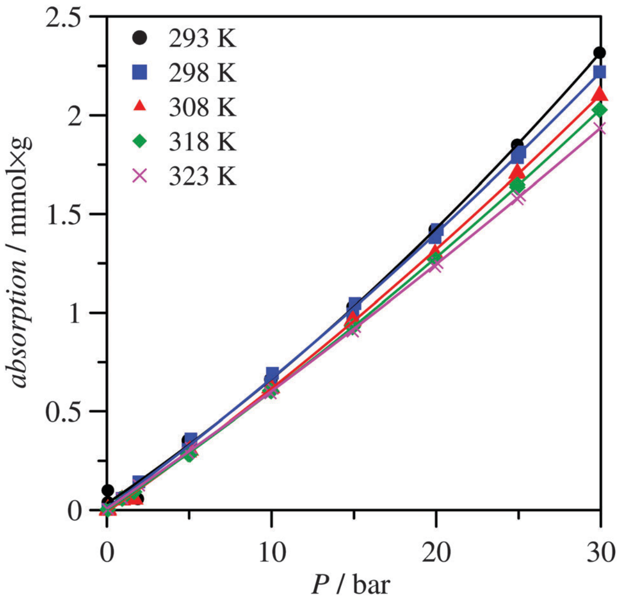

Fig. 7 High pressure CO_2 solubility in CHCL_LEV_1_2 DES system at various isotherms up to 30 bar. Points show experimental data and lines are plotted for guiding purposes.

with a positive curvature. During the solubility measurements, sorption hysteresis was also checked by conducting absorption/desorption cycle analysis. None of measurements at each isotherm did not show a sign of chemisorption, and weight measurements were obtained during the desorption along with the same absorption path. Moreover, in order to check whether there is a degradation of the sorption activity with the experimented DES system, each isotherm measurement was repeated three times and there was no significant absorption activity loss observed.

On the other hand, the kinetics of the absorption in the DES system has been investigated. Fig. 8 shows the amount of absorbed CO_2 in the DES system with time at both low and high pressures. At a pressure of 1 bar, an average time of 7 minutes was required to reach the equilibrium for a fully saturated DES solution. Whereas at 30 bar, 12 minutes passed before equilibrium conditions were reached.

3.7 Nanoscopic behavior from molecular dynamics

The forcefield parameterization used in this work was validated through the comparison of predicted physical properties with experimental values. Deviation between experimental and simulated density, ρ, data in the 298 to 348 K range are reported in Fig. 9. Density data from MD are slightly lower than experimental data, but are closer to those obtained by Florindo *et al.*[60] Nevertheless, deviations are lower than 0.9% in the whole temperature range, which show the suitable performance of the used parameterization for describing the macroscopic properties of the studied system. The temperature evolution of density, both for experimental and molecular dynamics predicted data, allows the obtaining of the isobaric thermal expansion coefficient, α_p, from its thermodynamic definition, leading to 0.583×10^{-3}, 0.576×10^{-3} and 0.593×10^{-3} K^{-1} at 298 K, for the experimental data obtained in this work, from Florindo *et al.*,[60] and from molecular dynamics simulations, respectively, which shows the excellent agreement between the simulated data and experimental values.

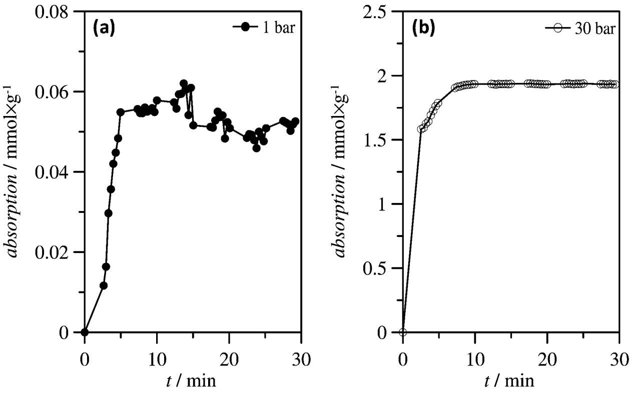

Fig. 8 Isobaric CO_2 solubility in CHCL_LEV_1_2 DES kinetics: (a) 1 bar and (b) 30 bar. Points show experimental data and lines are plotted for guiding purposes.

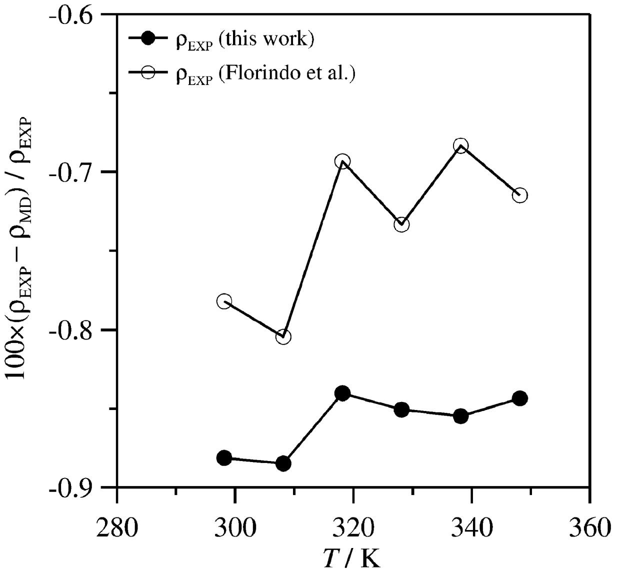

Fig. 9 Deviation between density data for CHCL_LEV_1_2 calculated from molecular dynamics simulations, ρ_{MD}, and experimental density, ρ_{EXP}, for experimental data obtained in this work and for data obtained by Florindo *et al.* ρ_{MD} at 1 bar and ρ_{EXP} at atmospheric pressure.

Self-diffusion coefficients were also calculated, using Einstein's equation from mean square displacements (msd), for all the involved molecules leading to values of 0.42×10^{-11} ($[CH]^+$), 0.68×10^{-11} ($[Cl]^-$), and 0.63×10^{-11} ([LEV]) $m^2\ s^{-1}$, at 298 K. The absence of experimental data hinders the comparison of simulated self-diffusion coefficients data; nevertheless, the $[CH]^+$ cation moves slower than $[Cl]^-$ and [LEV], which show similar mobilities at 298 K. Perkins *et al.*[99] reported self-diffusion data from molecular dynamics simulations of reline DES (composed of [CH][Cl] + urea in 1 : 2 molar ratio), their values being lower than those obtained in this work for CHCL_LEV_1_2 (roughly half) in agreement with the larger viscosity of reline in comparison with CHCL_LEV_1_2. Likewise, self-diffusion for $[CH]^+$ in reline is lower than for Cl^- and the corresponding HBD (urea), which is also in agreement with values for CHCL_LEV_1_2, but HBD in reline has larger molecular mobilities than that of $[Cl]^-$, whereas they have similar mobility in HCL_LEV_1_2. Perkins *et al.*[99] justified the self-diffusion data of $[Cl]^-$ and HBD in reline, indicating that in spite of the strong hydrogen bonding between both compounds their movements are not tied. On the contrary in the case of CHCL_LEV_1_2, the mobility of $[Cl]^-$ and HBD (LEV) seem to be strongly correlated.

A key point in the determination of self-diffusion coefficients from molecular dynamics simulations is if the condition of a fully diffusive regime is reached in the time frame used, which is commonly measured through the so-called β parameter, defined as the slope of log–log plots of msd *vs.* simulation time.

A fully diffusive regime is reached when $\beta = 1$ whereas subdiffusive regimes are characterized by $\beta < 1$. Perkins *et al.*[99] showed that in the case of reline at 298 K, a fully diffusive regime is reached at 30 ns, whereas it is reached at 10 ns for CHCL_LEV_1_2 in this work. This may be justified considering that reline viscosity[94] is twice that of CHCl_LEV_1_2, which leads to increased molecular mobilities (as shown by the larger self-diffusion coefficients) and thus diffusive regimes are reached at shorter simulation times. Dynamic viscosity was calculated using Green–Kubo method leading to 265 mPa s at 298 K, which is in fair agreement with 226.8 mPa s as obtained by Florindo *et al.*[60]

Vaporization enthalpy may be obtained from molecular dynamics simulations as the internal energy difference between liquid and gas phases (plus and $R \times T$ term), which can be assimilated to the difference between potential energies.[100,101] The gas phase was modeled considering a low density cage (0.006 g cm^{-3}) composed of a $[CH]^+$–$[Cl]^-$ ion pair and two LEV molecules not interacting with [CH][Cl]. In the course of gas phase simulations (10 ns long), LEV molecules aggregated with the [CH][Cl] ion pair. The main contributions to the CHCL_LEV_1_2 vaporization enthalpy at 298 K are summarized in Table 1, showing that the main contribution to the potential energy differences between liquid and gas phases is a non-bonded term arising from intermolecular interactions, whereas bonded and intra-molecular non-bonded terms are almost negligible. Likewise, the vaporization enthalpy of CHCL_LEV_1_2 is lower than those values reported in the literature for ionic liquids,[100] which is in agreement with the strong effect of strong coulombic effects arising in ionic liquids, whereas the strength of LEV–ions intermolecular interactions in the studied DES are weaker. This effect should be confirmed experimentally in future works.

The structure of CHCL_LEV_1_2 is strongly dominated by the strength and nature of intermolecular interactions, E_{inter}, and thus, intermolecular interaction energies are quantified and reported in Fig. 10. Anion–cation interactions are the stronger intermolecular interactions as may be expected considering their ionic nature. Regarding the ion–[LEV] interactions, it should be remarked upon that the positive E_{inter} values for $[Cl]^-$–[LEV], rising from the positive coulombic contribution because both molecules are negatively charged (see Methods section), in contrast with the larger and negative E_{inter} values (85% coulombic contribution) for $[CH]^+$–[LEV], both moderately decreasing with temperature. Nevertheless, the large total E_{inter} shows the development of very effective intermolecular interactions in the studied DES, which remains relatively constant in the studied temperature range. These results are in contrast with those obtained for reline by Sun *et al.*[102] which showed that $[Cl]^-$–HBD interactions are roughly three times larger than $[CH]^+$–HBD in the case of urea.

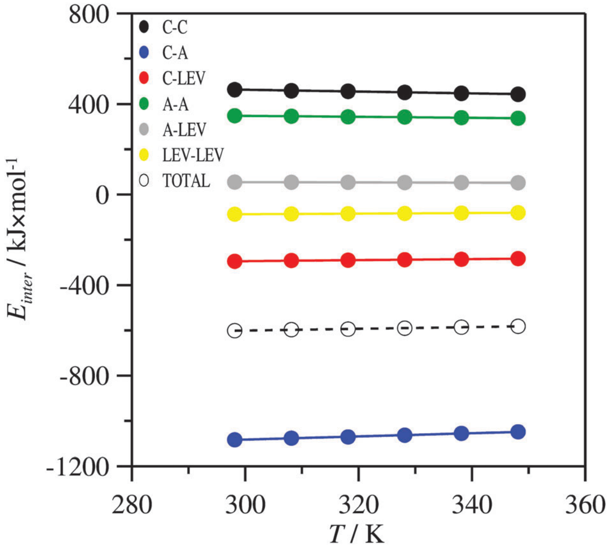

Fig. 10 Intermolecular interaction energies, E_{inter}, in CHCL_LEV_1_2 calculated from molecular dynamics simulations at different temperatures and a pressure of 1 bar. C stands for $[CH]^+$, A for Cl^-, LEV for levulinic acid, and TOTAL for the sum of all intermolecular interaction contributions. Lines show linear fits.

The main structural features for CHCL_LEV_1_2 may be obtained from the radial distribution functions, $g(r)$, reported in Fig. 11. The results in Fig. 11a show ion–ion interaction in CHCL_LEV_1_2. The anion–cation strong interaction describing the ion pair is well defined by the strong and narrow peak at short distance in Fig. 11a, whereas very minor features appear for this interaction at larger distances. Anion–anion interaction is characterized by a broad peak followed by a shoulder in the 5 to 10 Å range, which is in contrast with the cation–cation interactions, which are characterized by a strong intermolecular hydrogen bonding inferred from the narrow first peak in Fig. 11a followed by three weaker and wider peaks, which show that $[CH]^+$ develop well-defined hydrogen bonding through the cation hydroxyl group. For the analysis of ion–[LEV] interactions, it should be remarked that LEV has three sites that may act as donors and/or acceptors for hydrogen bonding: (i) the oxygen atom in –C=O of the –COO group, Ol1, (ii) the –OH in the –COO group, Ol2 and Hl, and (iii) the oxygen atom in the –CO terminal group, Ol3, Fig. 11. Radial distribution functions for these three groups are reported in Fig. 11b with regard to ion–[LEV] interactions. The results in Fig. 11b describe the hydrogen bonding with LEV both for the anion and cation, the $[Cl]^-$–[LEV] interaction (through the Hl site) leads to stronger peaks than $[CH]^+$–[LEV], but the $[Cl]^-$–[LEV] peak appears at a 0.3 Å larger distance, and thus this interaction should be weaker than for $[CH]^+$–[LEV]. The $[CH]^+$–[LEV] interactions are characterized by the development of hydrogen bonding between the $[CH]^+$ hydroxyl hydrogen, Hc, and the two possible acceptor sites in [LEV] (Ol1, and Ol3), which are characterized by well defined narrow peaks appearing at roughly 1.8 Å but

Table 1 Energy differences between liquid and gas phases for CHCL_LEV_1_2 calculated from molecular dynamics simulations. ΔH_{vap} is the vaporization enthalpy, $\Delta E_{\text{pot,BONDED}}$ is the bonded potential energy (bond, angle and dihedral contributions) difference, $\Delta E_{\text{pot,NON-BONDED}}$ is the non-bonded potential energy (Lennard-Jones and coulombic contributions) difference, $\Delta E_{\text{pot,TOT}}$ is the total potential energy difference and $\Delta E_{\text{pot,INTER}}$ is the intermolecular interactions potential energy difference. All values at 298 K

ΔH_{vap}/kJ mol^{-1}	$\Delta E_{\text{pot,TOT}}$/kJ mol^{-1}	$\Delta E_{\text{pot,BONDED}}$/kJ mol^{-1}	$\Delta E_{\text{pot,NON-BONDED}}$/kJ mol^{-1}	$\Delta E_{\text{pot,INTER}}$/kJ mol^{-1}
52.05	49.57	−4.76	54.34	40.74

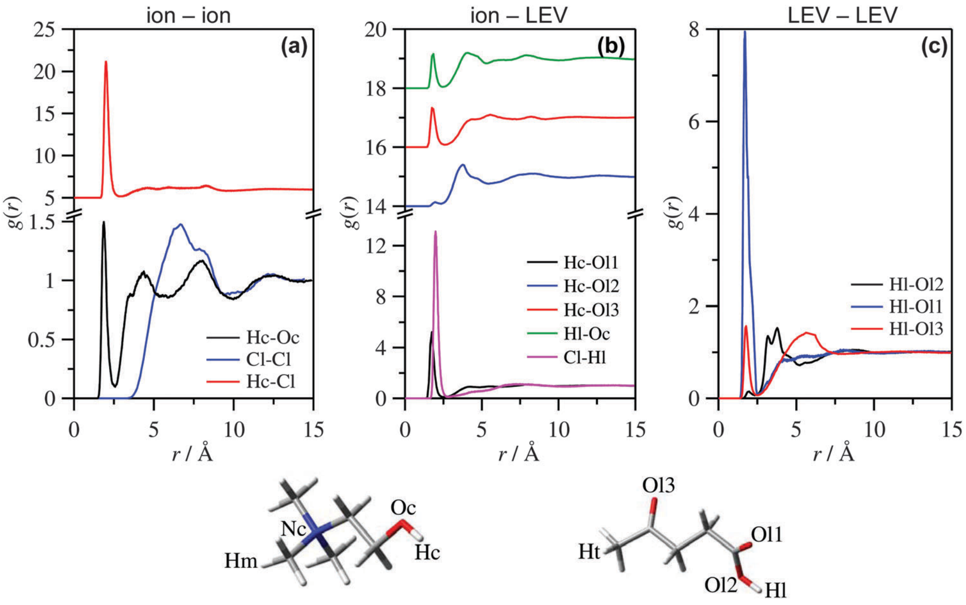

Fig. 11 Site–site radial distribution functions, $g(r)$, in CHCL_LEV_1_2 calculated from molecular dynamics simulations at 298 K and 1 bar.

being larger for the interaction through Ol1 site. The interaction through Ol2 has shown poor interactions according to the wide peak in Fig. 11b. Likewise, results in Fig. 11b show the development of $[CH]^+$–[LEV] hydrogen bonding in which [LEV] acts as a hydrogen bond donor, *via* Hl, and $[CH]^+$ as acceptor, *via* Oc, although being weaker than the situation in which [LEV] act as hydrogen bond acceptor.

Therefore, the $[CH]^+$–[LEV] interaction is mainly developed through the Ol1 site with weaker interactions through the Ol3 site and through Hl–Oc interaction. The [LEV]–[LEV] interaction is analyzed in Fig. 11c, showing that the main interaction is developed between the Hl and Ol1 sites, with weaker contributions arising from hydrogen bonding through the Ol3 position and almost negligible interactions through the Ol2 site. Therefore, the [LEV] hydroxyl group acts as a strong hydrogen bond donor, both with $[CH]^+$ and other [LEV] molecules, and the intermolecular hydrogen bonding is developed mainly through Ol1, and in minor extension, Ol3 acceptor sites.

A most detailed picture of the molecular arrangement in CHCL_LEV_1_2 can be obtained from spatial distribution functions, SDF, as reported in Fig. 12. The $[CH]^+$–$[CH]^+$ interaction is well defined in Fig. 12a showing the high density cap above the oxygen atom in the hydroxyl group (acceptor for H-bonds) and below the hydrogen atom in hydroxyl group (donor for H-bonds), together with a big cap surrounding the remaining $[CH]^+$ molecular regions showing the prevailing role of the hydroxyl group for the development of intermolecular hydrogen bonds. Cl^- anions develop a high-density region in the vicinity of the Hc group (Fig. 12b) in agreement with the strong peak in Fig. 11a. The arrangement of LEV Hl atoms around $[CH]^+$ (Fig. 12c) follows a similar pattern to that of Hc (Fig. 12a) showing that the [LEV] and $[CH]^+$ molecules occupy the same regions around a central $[CH]^+$ ion. Regarding the structuring around [LEV], the high density cap above the Ol1 atom of the Hc atom (Fig. 12d) shows that $[CH]^+$ cations tend to concentrate above the Ol1 in the LEV –COOH group, with weaker interactions through the remaining [LEV] H-bond acceptor sites. The $[Cl]^-$–[LEV] interactions are mainly developed

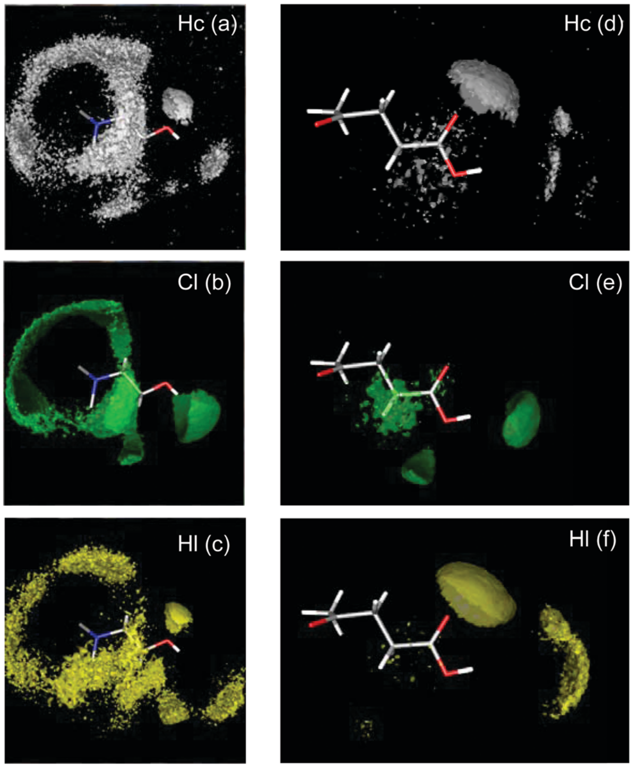

Fig. 12 Spatial distribution functions of relevant atoms around [CH] cation (panels a–c) and around LEV (panels d–f) in CHCL_LEV_1_2 calculated from molecular dynamics simulations at 298 K and 1 bar. All values show isodensity plots corresponding to 4-times bulk density. Atom names as in Fig. 14.

through the hydroxyl head group in [LEV] (Fig. 12d) but being placed at larger distances than in the case of Cl^- around $[CH]^+$. Finally, LEV–LEV interactions lead to high-density regions above the Ol1 group (Fig. 12e).

The structural features inferred from Fig. 11 and 12 show the development of H-bonding between all the involved molecules through the $[CH]^+$ hydroxyl site and LEV –COOH group, and thus, the number of H-bonds is reported in Fig. 13. A large number of H-bonds is developed with the $[Cl]^-$ anion both through the Hc ($[CH]^+$) and Hl (LEV) sites, being larger for $[LEV]–[Cl]^-$. The number of $[CH]^+–[CH]^+$ H-bonds (Hc–Oc) is lower than that for $[CH]^+$–[LEV] (Hc–Ol1, Hc–Ol2 and Hc–Ol3), which are larger for the Hc–Ol1 site as expected from the results in Fig. 14b, and in agreement with results in Fig. 12a and d. [LEV]–[LEV] H-bonds are developed mainly through the Ol1 site with minor interactions through the Ol3 site and there is negligible H-bonding through Ol2 site. These results should be analyzed considering that the two LEV molecules interact with a central $[Cl]^-$ anion, and thus, this leads to larger LEV–LEV and $[CH]^+$–LEV H-bonding.

The development of strong H-bonding between all the involved molecules in CHCL_LEV_1_2 requires an additional analysis of the lifetimes of these intermolecular interactions. This analysis was carried out through the calculation of residence time, t_{res}, of relevant sites around others in order to characterize H-bonding. Residence time was calculated from the exponential decay of the conditional probability for a site to stay within a sphere of defined radius around another molecular site, as explained in previous work.[103] Sun *et al.*[102] reported lifetimes of hydrogen bonds in reline DES, showing lifetimes lower than 13 ps for all the reported H-bonds in the eutectic composition, with values of 12.574 ps for the $[CH]^+–Cl^-$ H-bond, 2.397 ps for the urea (HBD)–$[Cl]^-$ H-bond, and 2.952 ps for the urea–urea interaction. These values are lower than those reported for CHCL_LEV_1_2 in Fig. 14a, but it may be argued that the distance criteria used to define residence times in Fig. 14a (6.0 Å) is roughly double that used by Sun *et al.*[102] to define their H-bond lifetimes (roughly 3 Å). The criteria used in Fig. 14 consider the existence of a second solvation shell around each hydrogen bond donor site, and thus, although H-bonds are destroyed for distances larger than 3.0 Å, those atoms reamining in the 3–6 Å range arise from the reorganization of the local H-bonding structure and they may develop a new H-bond in a fast way, and thus using 6.0 Å may give a realistic picture of the H-bonding around a certain site. The residence times reported in Fig. 14a are very similar for all the considered interactions being in the 35 to 55 ps range. Moreover, the analysis of the temperature evolution of residence times follows a similar non-Arrhenius pattern for all the studied interactions, thus confirming a strong correlation between the dynamics of all the studied H-bonds.

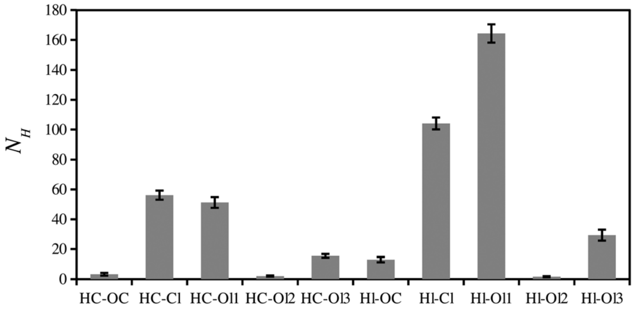

Fig. 13 Number of hydrogen bonds, N_H, between the different donor–acceptor interaction sites for CHCL_LEV_1_2 calculated from molecular dynamics simulations. Values calculated for a simulation box containing 250 [CH][Cl] ion pairs and 250 LEV molecules. Reported values show averages in the 298 K to 348 K temperature range with error bars showing standard deviations for that temperature range. All values calculated considering 3.0 Å and 50.0° as donor–acceptor distance and angle cut-offs, respectively.

The results in Fig. 15 show the changes in intermolecular interaction energy upon CO_2 absorption for CO_2 pressures up to 10 bar. The structure of CHCL_LEV_1_2 does not change upon CO_2 absorption from an energetic viewpoint; ion–ion, ion–LEV and LEV–LEV E_{inter} suffer very minor changes with increasing CO_2 mole fraction (Fig. 15a) (*e.g.* for $[CH]^+–[Cl]^-$, E_{inter} decreases just a 2.5% in absolute value). Therefore the liquid structure of CHCL_LEV_1_2 is able to accommodate CO_2 molecules without remarkable changes in its mechanism of intermolecular interaction. Regarding the strength of the interactions between CO_2 and molecules present in CHCL_LEV_1_2, the results in Fig. 15b show that the strength of interactions

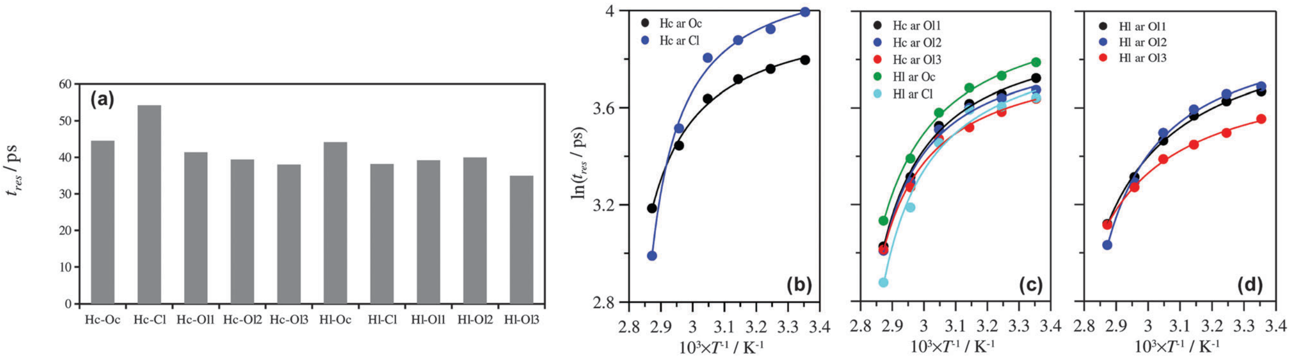

Fig. 14 Residence time, t_{res}, of selected atoms around other atoms in DES_LEV_1_2. t_{res} was calculated from the exponential decay of conditional probability P with R = 6.0 Å.

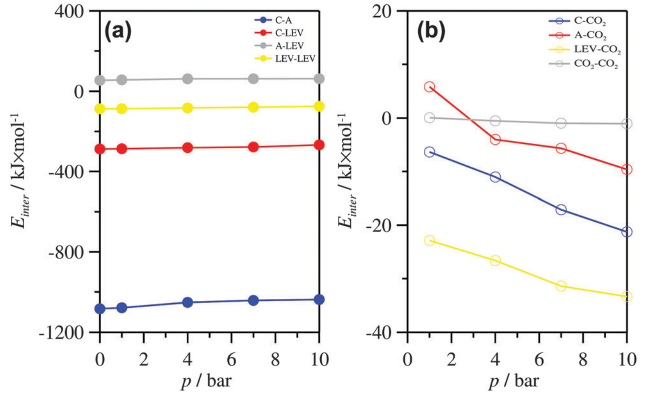

Fig. 15 Intermolecular interaction energies, E_{inter}, in the CHCL_LEV_1_2 + CO_2 systems calculated from molecular dynamics simulations at different CO_2 pressures and 298 K. C stands for $[CH]^+$, A for Cl^-, LEV for levulinic acid. Lines are plotted for guiding purposes.

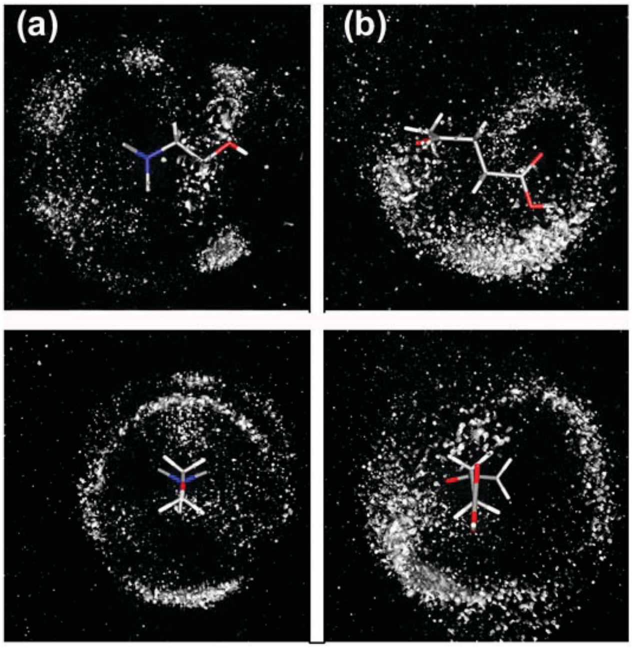

Fig. 17 Spatial distribution functions of CO_2 carbon atoms around (a) $[CH]^+$ and (b) LEV, in CHCL_LEV_1_2 + CO_2 systems calculated from molecular dynamics simulations at a CO_2 pressure of 10 bar and 298 K. All values show isodensity plots corresponding to 4-times bulk density.

follow the ordering [LEV] > $[CH]^+$ > $[Cl]^-$, and thus point to a preferential absorption of CO_2 molecules through interaction with LEV molecules. The structural features of CO_2 absorption are summarized in Fig. 16 for radial distribution functions. The arrangement of CO_2 molecules around $[CH]^+$ (Fig. 16a) show that CO_2 molecules are placed both around the cation hydroxyl group and also around the methyl groups, following a similar pattern for the first solvation sphere, although for the hydroxyl group two additional maxima in $g(r)$ points to a slightly stronger interaction through that site. This is confirmed by spatial distribution functions as shown in Fig. 17a, which although they show high density caps around the $[CH]^+$ hydroxyl group, they also show a very symmetrical distribution of CO_2 molecules around the methyl group, which would justify the sharp and narrow peak around the $[CH]^+$ nitrogen atom in $g(r)$ as shown in Fig. 17a. The CO_2 molecules are also strongly structured around $[Cl]^-$ (Fig. 17b), the sharp peak in $g(r)$ following a similar pattern to the interaction between CO_2 molecules and the Hc site in $[CH]^+$; therefore as the absorption of CO_2 molecules does not disrupt anion–cation interactions, CO_2 may interact efficiently with both ions at the same time. The CO_2–[LEV] interaction is characterized by the strong features in $g(r)$ around the Hl and Ol3 sites, with weaker interactions through the Ol3 site, leading to a CO_2 distribution around the terminal [LEV] methyl group. Therefore, CO_2 molecules are placed around the LEV hydroxyl group and also around the terminal groups of the [LEV] molecule (Fig. 17b) with minor concentration around the Ol1 group.

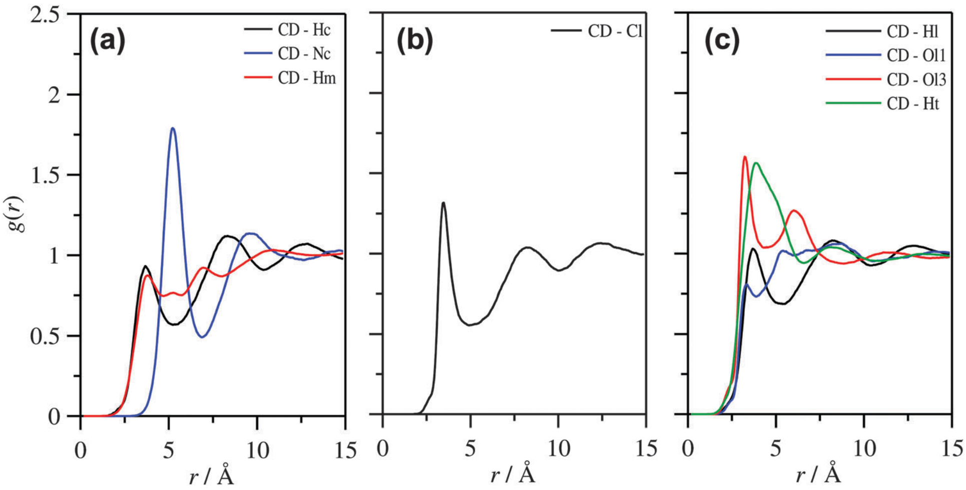

Fig. 16 Site–site radial distribution functions, $g(r)$, in CHCL_LEV_1_2 + CO_2 systems calculated from molecular dynamics simulations at a CO_2 pressure of 10 bar and 298 K. Atom names as in Fig. 14; CD stands for carbon atoms in CO_2, Hm stands for all the hydrogen atoms in methyl groups bonded to the Nc atom in $[CH]^+$; Ht stands for all the hydrogen atoms in methyl group of LEV.

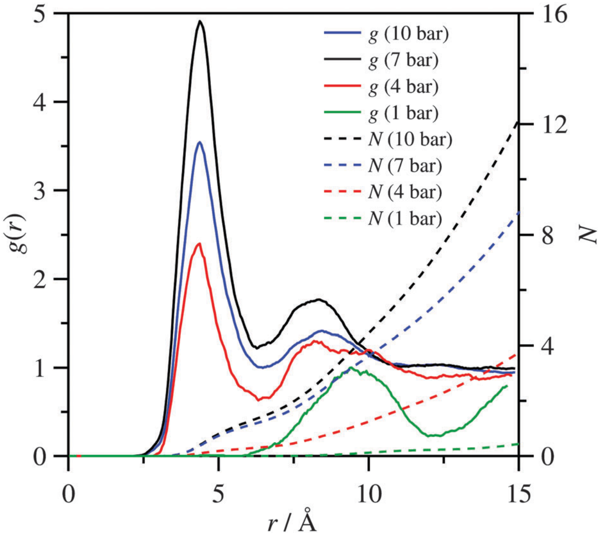

Fig. 18 CD–CD site–site radial distribution functions, $g(r)$, in CHCL_LEV_1_2 + CO_2 systems calculated from molecular dynamics simulations as a function of CO_2 pressure at 298 K. CD stands for carbon atoms in CO_2.

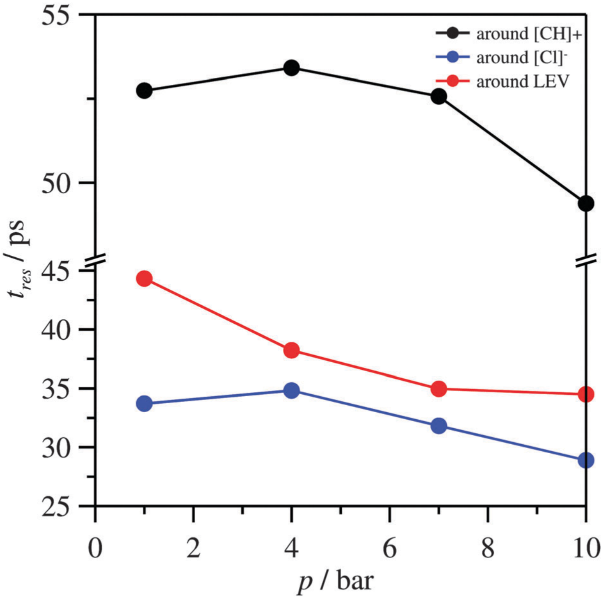

Fig. 19 Residence time, t_{res}, of CO_2 carbon atoms around the center of mass of $[CH]^+$, $[Cl]^-$, and LEV molecules in CHCL_LEV_1_2 + CO_2 systems calculated from molecular dynamics simulations as a function of CO_2 pressure, p, at 298 K. CD stands for carbon atoms in CO_2. t_{res} was calculated from the exponential decay of conditional probability P with R = 6.0 Å.

Upon increasing the absorbed amounts of CO_2, these molecules tend to form clusters. At a CO_2 pressure of 1 bar, the number of absorbed molecules is very low and thus CO_2 clusters were not observed (Fig. 18), but with increasing CO_2 mole fraction (increasing pressure) a well defined peak at 4.3 Å in $g(r)$ is obtained followed by a second and wider peak. The position of these peaks does not change with increasing pressure, only their intensity increases with increasing amounts of absorbed CO_2. The corresponding running integrals for these $g(r)$ show that the first solvation sphere, integrating up to the first minimum, around a central CO_2 molecule contains at least two additional CO_2 molecules, whereas another two additional CO_2 molecules may be found in the second solvation sphere for the highest studied pressures.

The dynamics of CO_2 absorbed molecules may be analyzed considering the residence times of CO_2 around both ions and [LEV] molecules, as shown in Fig. 19. The results show that the mobility of CO_2 molecules is almost twice around $[Cl]^-$ and [LEV] than that around $[CH]^+$, and in all the cases these mobilities increase with increasing CO_2 pressure, with the exception of the change from 1 to 4 bar. This result is surprising considering the strength of the interactions between CO_2 molecules and CHCL_LEV_1_2 molecules as reported in Fig. 15b — which led to larger E_{inter} for CO_2–LEV than for the other interaction pairs — but it may be explained considering steric factors around the $[CH]^+$ which hinder the molecular mobility of CO_2 molecules interacting with this ion in comparison with the CO_2 absorption sites around LEV.

A remarkable feature that should be analyzed in order to understand the mechanism of absorption of CO_2 molecules in CHCL_LEV_1_2, is the interfacial behavior of CHCL_LEV_1_2–CO_2 systems. The CO_2 capture from flue gases requires that CO_2 molecules are adsorbed at the sorbent–gas interface and then they diffuse from the interfacial region toward the bulk DES. Therefore, to analyze this process step a simulation on the properties of the CO_2–DES interface was carried out using molecular dynamics in this work. Pure CO_2 gas was put in contact with CHCL_LEV_1_2 and the behavior was followed as a function of time. For comparison purposes the CHCL_LEV_1_2–vacuum interface was also simulated. The density profiles shown in Fig. 20a–c allow the characterization of the molecular arrangements of ions and LEV molecules in the interfacial region with vacuum. The density profiles for ions and LEV center-of-mass in Fig. 20a show that [LEV] molecules occupy outer regions close to the vacuum layer with ions being placed in inner regions, therefore, the CHCL_LEV_1_2–vacuum interface is composed mainly of [LEV] molecules (Fig. 21a). Fig. 20b shows that $[CH]^+$ cations tend to orientate themselves parallel to the interface, whereas results in Fig. 20c show how [LEV] molecules are placed perpendicular to the vacuum interface with the –COOH group pointing toward the bulk fluid and the terminal methyl group exposed to the vacuum layer. These molecular arrangements do not change significantly when CHCL_LEV_1_2 is put in contact with a CO_2 gas layer. Very subtle structural changes occur to accommodate adsorbed CO_2 molecules at the interface (Fig. 20d–f), but ion and LEV arrangements are similar to those at the vacuum interface (Fig. 21b).

The main structural feature of the CHCL_LEV_1_2–CO_2 interface is the formation of a strongly adsorbed layer of gas molecules (Fig. 21b) which is formed in the first stages of the simulations (0 to 1 ns); then upon the formation of this initial layer its size increases upon increasing simulation time (Fig. 22). The main characteristic of this adsorbed layer is that CO_2 molecules are adsorbed very quickly but once they are in this layer above CHCL_LEV_1_2, in contact mainly with [LEV] molecules, their mobility is significantly reduced, and thus the

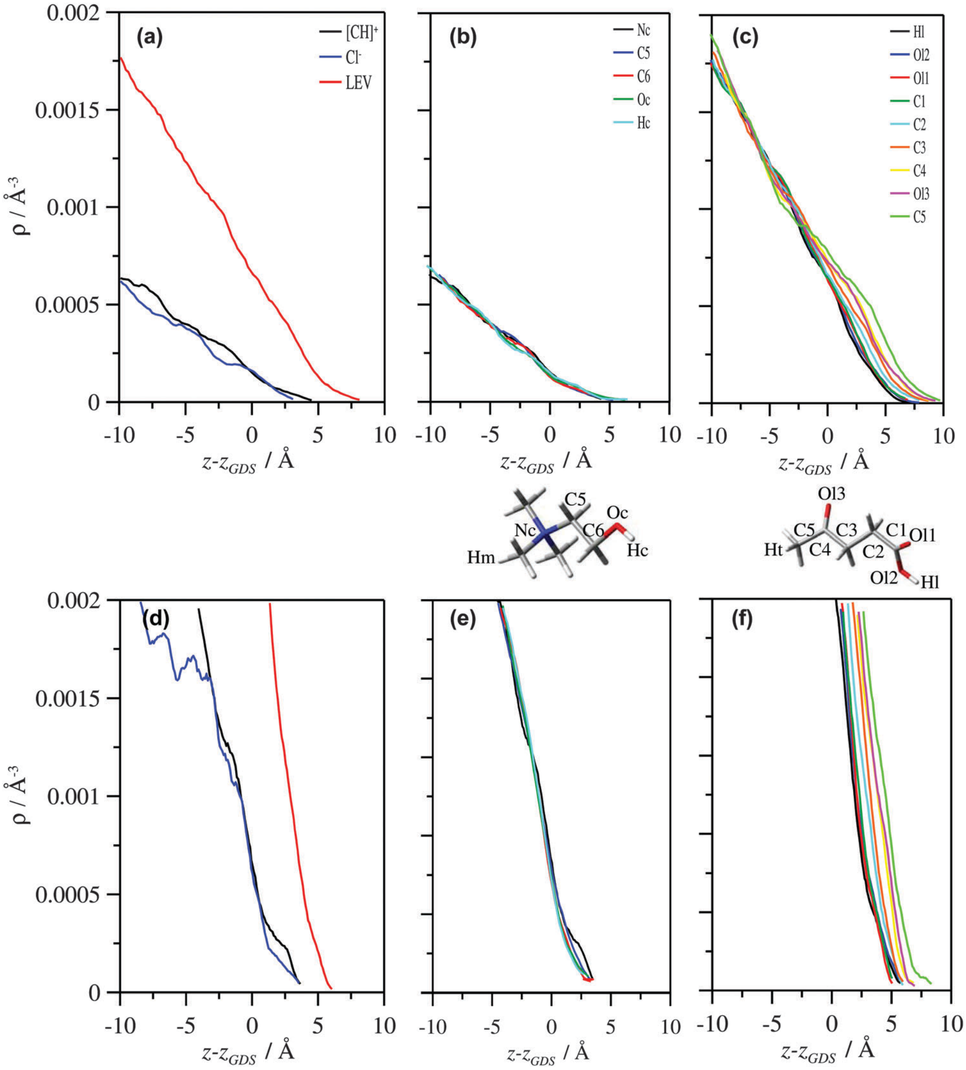

Fig. 20 Density profiles for (a and d) center of mass of $[CH]^+$, Cl^- and LEV, and for relevant atoms in (b and e) $[CH]^+$ and (c and f) LEV, molecules in CHCL_LEV_1_2 + (a–c) vacuum and (d–f) CO_2 interfaces systems calculated from molecular dynamics simulations at 298 K. z stands for the coordinate perpendicular to the corresponding interfaces, and z_{GDS} for the coordinate of the Gibbs dividing surface. Profiles obtained as averages in the 4 to 5.5 ns timeframe.

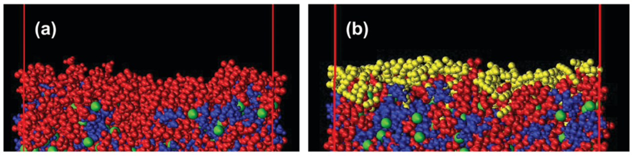

Fig. 21 Snapshot of the CHCL_LEV_1_2–(a) vacuum or (b) CO_2 interfaces calculated from molecular dynamics simulations at 298 K. Color code: (blue) $[CH]^+$, (green) Cl^-, (red) LEV, and (yellow) CO_2. Snapshots obtained after 5.5 ns simulations.

time that CO_2 molecules remain in this layer on top of CHCL_LEV_1_2 is long (Fig. 22). In the first 6 ns of simulation, all the CO_2 molecules were placed in the adsorbed layer whereas no CO_2 molecules were able to diffuse toward the bulk CHCL_LEV_1_2. The layer of CO_2 adsorbed molecules develop strong interactions with [LEV] molecules and weaker ones with $[CH]^+$, especially when the adsorbed layer is wide enough (simulation times > 4 ns, Fig. 23), which is in agreement with the interface structure inferred from Fig. 20a. This persistence of the CO_2 molecules in the initially adsorbed layer at the CHCL_LEV_1_2–gas interface before moving toward the bulk liquid phase should be considered for any industrial application of this DES as a carbon capture agent. The kinetics of the CO_2 absorption process (largely controlled by the high affinity of CO_2 molecules for the [LEV]-rich interfacial region) has to be analyzed together with thermodynamic factors controlling the capturing process.

3.8 Short-range properties through DFT

Previously, CHCL_LEV_1_2 structural features and CO_2 capture mechanism have been analyzed in the context of MD simulations. In this section, the main features relating to CHCL_LEV_1_2 and CHCL_LEV_1_2$\cdots CO_2$ systems are assessed trough DFT simulations. The bulk effects that are studied though DFT simulations

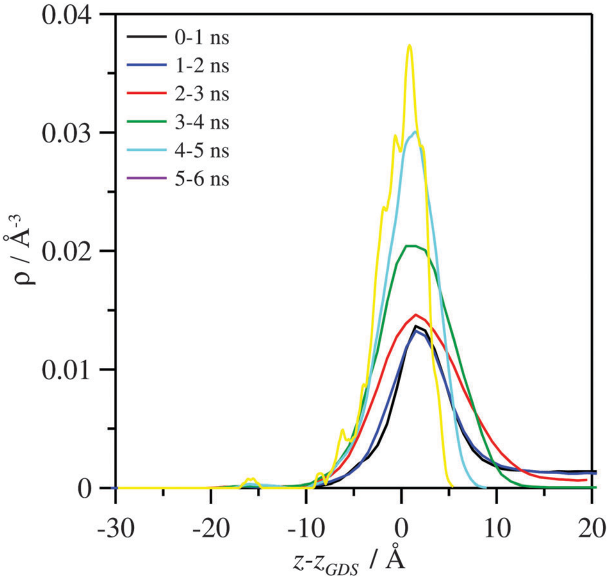

Fig. 22 Density profiles for CO_2 molecules in CHCL_LEV_1_2 + CO_2 interface system calculated from molecular dynamics simulations at 298 K. z stands for the coordinate perpendicular to the corresponding interfaces, and z_{GDS} for the coordinate of the Gibbs dividing surface. Profiles obtained as averages in the reported timeframes.

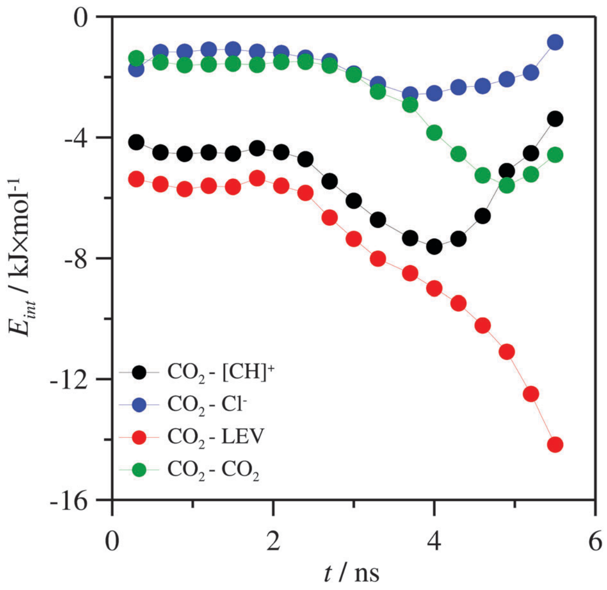

Fig. 23 Intermolecular interaction energy, E_{int}, between CO_2 and molecules forming CHCL_LEV_1_2 + CO_2 interface system as a function of simulation time, calculated from molecular dynamics simulations at 298 K.

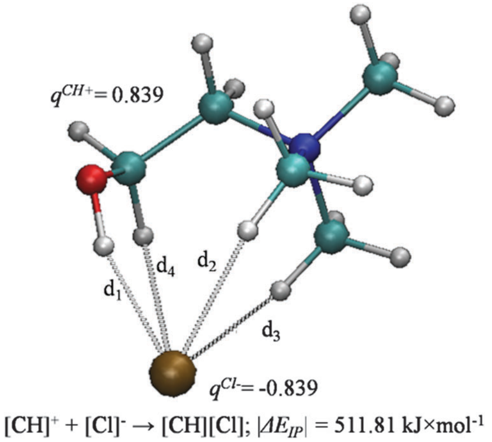

Fig. 24 Optimized structures for [CH][Cl] at B3LYP-D2/6-31+G** level, along with the main structural parameters related with intermolecular interactions. Computed charges over choline (q^{CH^+}) and chloride (q^{Cl^-}) motifs, as well as the binding energy (ΔE_{IP}) for the ionic pair interaction are also shown.

allow detailed insights of the studied systems at the molecular level which is useful for forecasting macroscopic behavior. Fig. 24–26 show optimized structures for [CH][Cl], CHCL_LEV_1_2 and CHCL_LEV_1_2$\cdots$$CO_2$ systems, respectively. In Table 2 is listed distances for those intermolecular interactions found in the context of AIM theory, along with the electronic density value (ρ) for the corresponding BCP. Prior to analyzing the CHCL_LEV_1_2 and CHCL_LEV_1_2$\cdots$$CO_2$ systems, this paragraph discusses the main features for the [CH][Cl] ionic compound (Fig. 24). As expected, the main interaction between both ions is due to a coulombic attraction between both ions, which agrees with the high binding energy for the ionic pair interaction, $|\Delta E_{IP}|$ = 511.81 kJ mol^{-1}. For the ionic pair, the intermolecular charge transfer (CT_{IP}) is equal to 0.161e$^-$. In addition, the chloride anion stabilizes four intermolecular hydrogen bonds with the cation (d_1–d_4), wherein the strongest H-bond is *via* the OH (cation) group.

In accordance with MD simulations, the optimized structure for CHCL_LEV_1_2 (Fig. 15) is mainly characterized by intermolecular hydrogen bonds between the chloride atom and both levulinic acid molecules. Both levulinic acid molecules H-bond (through H atom of COOH group) with the chloride atom (d_5 and d_6 for LEV1 and LEV2, respectively). In addition, both molecules also establish several H-bonds with the choline cation. All these bonds (d_7, d_8 and d_9, d_{10} for LEV1 and LEV2, respectively) are formed through the COOH group (levulinic acid) and methylic hydrogen atoms (choline), except d_7, which is formed between the COOH group and the –CH_2 group adjacent to the OH motif. As can be seen in Table 2, Cl^-–LEV interactions yield the largest electronic density values, *i.e.*, the key interactions in the DES structure are those carried out between the levulinic molecules and the chloride atoms. The interaction energy between the ionic pair and the [LEV] molecules was $|\Delta E_{DES}|$ = 141.93 kJ mol^{-1} (Fig. 25), favorable lower energy state DES structure. Fig. 25 also shows the computed charges over cation, anion and levulinic acid motifs. The largest change on the charges is noted for the chloride atom, which decreases its charge 0.155e$^-$ (relative to the [CH][Cl] ionic pair). For CHCL_LEV_1_2 some negative charge is transferred from the anion up to the levulinic acid molecules, 0.066e$^-$ and 0.074e$^-$ for LEV1 and LEV2, respectively. In addition, there are also some hydrogen bonds between both ions, very similar to those reported in Fig. 24. In this sense, the chloride atom forms three hydrogen bonds (d_1–d_3) with the cation, which are

Table 2 Intermolecular distances along with their corresponding electronic density (ρ) values for the main intermolecular interactions for [CH][Cl], CHCL_LEV_1_2 and CHCL_LEV_1_2$\cdots$CO$_2$ systems estimated at DFT/B3LYP-D2/6-31+G** theoretical level. See Fig. 17–19. Estimated binding energies are also collected

		Length/Å	ρ/a.u.		Length/Å	ρ/a.u.	ΔE/kJ mol^{-1}
[CH][Cl]	d_1	2.084	0.0341	d_3	2.418	0.0184	$\lvert\Delta E_{IP}\rvert = 511.81$
	d_2	2.383	0.0197	d_4	2.809	0.0104	
CHCL_LEV_1_2	d_1	2.241	0.0233	d_7	2.317	0.0132	$\lvert\Delta E_{DES}\rvert = 141.93$
	d_2	2.626	0.0120	d_8	2.528	0.0099	$\lvert\Delta E_{IP}\rvert = 503.83$
	d_3	2.637	0.0116	d_9	2.366	0.0113	
	d_5	2.069	0.0331	d_{10}	2.375	0.0117	
	d_6	2.088	0.0315				
CHCL_LEV_1_2$\cdots$CO$_2$ (a)	d_1	2.247	0.0230	d_8	2.526	0.0100	$\left\lvert\Delta E^{a}_{DES-CO_2}\right\rvert = 17.46$
	d_2	2.646	0.0115	d_9	2.381	0.0112	$\lvert\Delta E^{a}_{DES}\rvert = 140.18$
	d_3	2.661	0.0110	d_{10}	2.377	0.0114	$\lvert\Delta E^{a}_{IP}\rvert = 503.03$
	d_5	2.076	0.0329	d_{11}	3.468	0.0050	
	d_6	2.098	0.0307	d_{12}	2.960	0.0082	
	d_7	2.351	0.0122				
CHCL_LEV_1_2$\cdots$CO$_2$ (b)	d_1	2.241	0.0232	d_7	2.325	0.0130	$\left\lvert\Delta E^{b}_{DES-CO_2}\right\rvert = 5.93$
	d_2	2.666	0.0112	d_8	2.511	0.0101	$\lvert\Delta E^{b}_{DES}\rvert = 140.12$
	d_3	2.632	0.0117	d_9	2.471	0.0094	$\lvert\Delta E^{b}_{IP}\rvert = 503.39$
	d_5	2.073	0.0329	d_{10}	2.383	0.0113	
	d_6	2.066	0.0332	d_{13}	2.733	0.0128	
CHCL_LEV_1_2$\cdots$CO$_2$ (c)	d_1	2.246	0.0230	d_8	2.503	0.0102	$\left\lvert\Delta E^{c}_{DES-CO_2}\right\rvert = 3.52$
	d_2	2.628	0.0120	d_9	2.363	0.0115	$\lvert\Delta E^{c}_{DES}\rvert = 139.10$
	d_3	2.630	0.0118	d_{10}	2.360	0.0120	$\lvert\Delta E^{c}_{IP}\rvert = 503.51$
	d_5	2.080	0.0322	d_{14}	3.446	0.0051	
	d_6	2.092	0.0317	d_{15}	2.949	0.0078	
	d_7	2.311	0.0133				

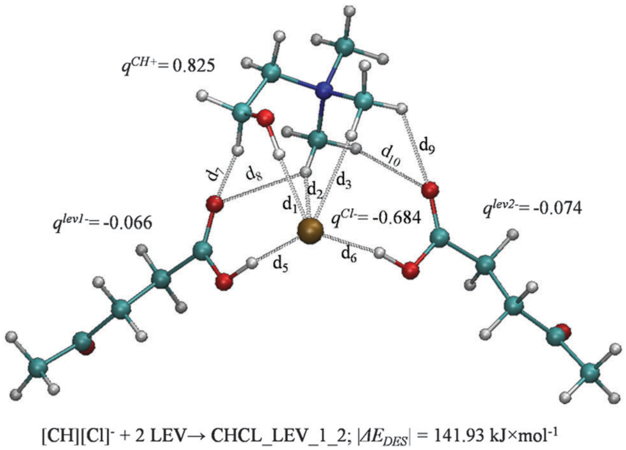

Fig. 25 Optimized structures for CHCL_LEV_1_2 at B3LYP-D2/6-31+G** level, along with the main structural parameters related with intermolecular interactions. Computed charges over choline (q^{CH^+}), chloride (q^{Cl^-}) and levulinic (q^{Lev}) motifs, as well as the binding energy (ΔE_{DES}) corresponding to DES formation are also shown.

weakened compared with the ionic compound. Thus, d_1 suffers an elongation of 0.157 Å, while its electronic density value is diminished by 0.0108 a.u. From the CHCL_LEV_1_2 optimized structure, the binding energy for the ionic pair has been also calculated through a single point calculation, which is also used for estimating the interaction strength. For CHCL_LEV_1_2, $\lvert\Delta E_{IP}\rvert$ = 503.87 kJ mol^{-1}, *i.e.* DES formation results in a waning of the ionic pair interaction of around 7.93 kJ mol^{-1}.

Fig. 26 shows the optimized structure for CHCL_LEV_1_2$\cdots$CO$_2$. Three different arrangements (a, b, and c) were found for the interaction between the DES and the CO$_2$ molecule. As noted from MD simulations, the structure of CHCL_LEV_1_2 does not change upon CO$_2$ absorption. In this sense, the same intermolecular H-bonds reported for the DES structure (d_1–d_{10}) were also found in presence of a CO$_2$ molecule. As can be seen in Table 2, intermolecular distances and their electronic density values change slightly in presence of the CO$_2$ molecule. ΔE_{IP} and ΔE_{DES} were also computed for the CHCL_LEV_1_2$\cdots$CO$_2$ optimized structures. For these arrangements, $\lvert\Delta E_{IP}\rvert \simeq$ 503.30 kJ mol^{-1} and $\lvert\Delta E_{DES}\rvert \simeq$ 139.80 kJ mol^{-1}, very similar than those values computed for CHCL_LEV_1_2. There are some similarities between arrangements a and c. From a structural viewpoint, for arrangement a/c, the CO$_2$ molecule is mainly linked to the Cl atom (d_{11}/d_{14}) and the COOH group of LEV1/LEV2 (d_{12}/d_{15}), the latter having the largest electronic density values for the associated BCP. In addition, d_{11}/d_{12} features are similar to d_{14}/d_{15}. Nevertheless, $\left\lvert\Delta E^{a}_{DES-CO_2}\right\rvert$ (17.46 kJ mol^{-1}) is larger than $\left\lvert\Delta E^{b}_{DES-CO_2}\right\rvert$ (14.77 kJ mol^{-1}). This energy difference could be related to the different charge distributions. For arrangement a, LEV1 is more negative than LEV1 in CHCL_LEV_1_2, which allows a slightly larger charge transfer up to the CO$_2$

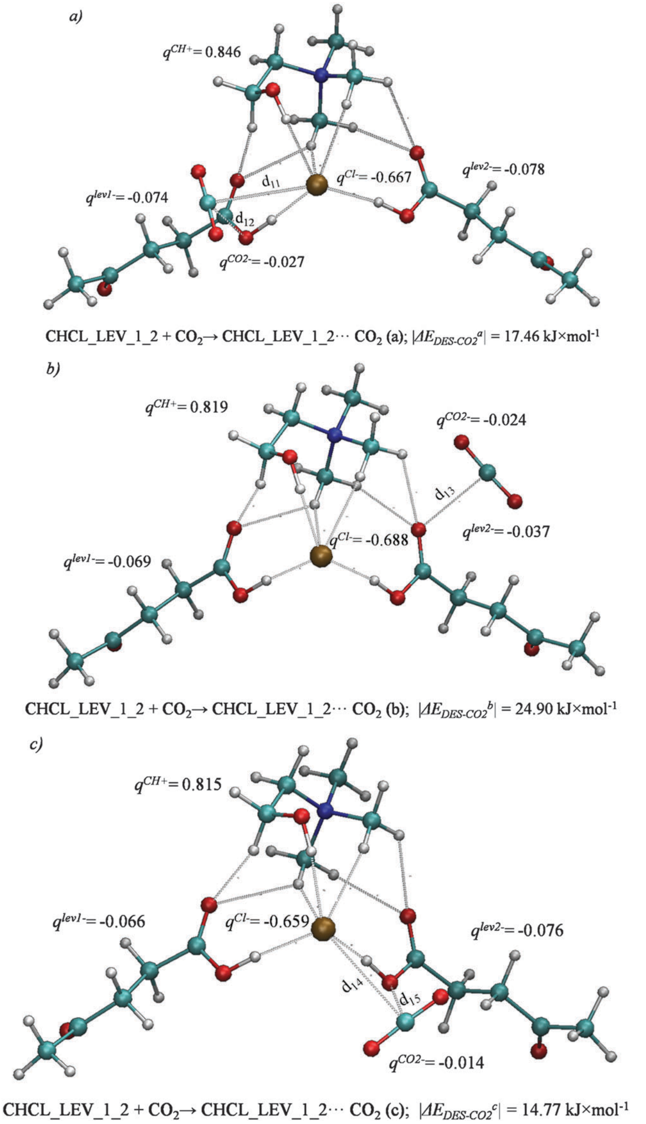

Fig. 26 Optimized structures for CHCL_LEV_1_2···CO$_2$ system (three different arrangements were found) at B3LYP-D2/6-31+G** level, along with the main structural parameters related with intermolecular interactions. Computed charges over choline (q^{CH^+}), chloride (q^{Cl^-}), levulinic (q^{Lev}) and CO$_2$ (q^{CO2}) motifs, as well as the binding energy ($\Delta E_{\mathrm{DES-CO_2}}$) corresponding to CO$_2$ capture by DES are also shown. For clarity, intermolecular bond labels corresponding to DES have been omitted, since we followed the same nomenclature used in Fig. 25.

molecule (whose charge is 0.027e$^-$). However, the negative charge over LEV2 in arrangement c does not vary, the charge transfer up to CO$_2$ molecule being around 0.014e$^-$. As far as the Cl charge is concerned, the largest charges are noted for arrangement c. With regard to arrangement b, the CO$_2$ molecules are mainly interacting with the COOH group of LEV2, through d$_{13}$ which is stronger (based on lower/larger intermolecular distances/electronic density values, respectively) than those interactions found in arrangements a and c. Although the charge over LEV2 is still very small, LEV2 decreases its charge 0.037e$^-$, while for the charges over LEV1, choline and chloride remain unaffected. These interactions provide the largest binding energies for CO$_2$ capture, $\left|\Delta E^{\mathrm{c}}_{\mathrm{DES-CO_2}}\right| = 24.90\ \mathrm{kJ\ mol^{-1}}$. According to the DFT results, CHCL_LEV_1_2 displays three different positions for CO$_2$ absorption, whose high values would indicate that this is an energetically favored process.

4. Conclusions

This extensive study combines both experimental and theoretical investigation of the DES system made by mixing CHCl and LEV with a 1 : 2 mixing ratio. Experimental studies are focused on obtaining detailed physical characteristics of the studied system; and CO$_2$ solubility at high pressures was the most important part of the experimental study. A promising absorption of 2.316 mmol of CO$_2$ per gram of DES sample at 293 K has been obtained at a pressure of 50 bar. Moreover, a detailed corrosivity study that deals with the CO$_2$ saturated DES system demonstrated a great corrosion resistance, with a corrosion rate of 0.027 mm year^{-1}, whereas the same experiments showed a corrosion rate of 0.54 mm year^{-1} for the CO$_2$ saturated MEA system.

Molecular dynamics and DFT results allowed the analysis of the structural properties of CHCL_LEV_1_2, both in the pure state and after CO$_2$ absorption. The CHCL_LEV_1_2 liquid phase is characterized by the development of intermolecular hydrogen bonding between [LEV] molecules and both Cl$^-$ and [CH]$^+$ ions, with [LEV] molecules mainly accepting H-bonds through the Ol1 atom in the –COOH group and also acting as a H-bond donor through the hydrogen atom of the hydroxyl group. Likewise, [CH]$^+$ is also self associated through H-bonding, and thus the characteristics of the functional groups available in the molecules comprising CHCL_LEV_1_2 allow the development of a very efficient network of H-bonds, which is the main reason for the properties of this fluid. This structuring does not change upon CO$_2$ absorption for pressures lower than 10 bar, with the CO$_2$ molecules developing stronger interactions with [LEV] molecules than with the ions. The CO$_2$ capture process by CHCL_LEV_1_2 is also characterized by the strong affinity of CO$_2$ molecules for the interfacial DES–gas region, which is very rich in [LEV] molecules, thus leading to large lifetimes of the adsorbed molecules in the interfacial region with slow migration toward the bulk fluid region.

The combined experimental and computational results reported in this work allow a detailed characterization of CHCL_LEV_1_2 DES, from both macroscopic and nanoscopic viewpoints, and demonstrate its suitability for possible use as carbon capture agent.

Acknowledgements

This work was made possible by NPRP grant # 6-330-2-140 from the Qatar National Research Fund (a member of Qatar Foundation), Ministerio de Economía y Competitividad (Spain, project CTQ2013-40476-R) and Junta de Castilla y León (Spain, project BU324U14). Gregorio García acknowledges the funding by Junta de Castilla y León, cofunded by European Social Fund, for a postdoctoral contract. We also acknowledge The Foundation of Supercomputing Center of Castile and León (FCSCL, Spain), Computing and Advanced Technologies Foundation of Extremadura (CénitS, LUSITANIA Supercomputer, Spain), and Consortium of Scientific and Academic Services of Cataluña (CSUC, Spain) for providing supercomputing facilities. The statements made herein are solely the responsibility of the authors.

References

1 B. Li, Y. Duan, D. Luebke and B. Morreale, *Appl. Energy*, 2013, **102**, 1439–1447.

2 N. von der Assen, J. Jung and A. Bardow, *Energy Environ. Sci.*, 2013, **6**, 2721–2734.

3 R. Wennersten, Q. Sun and H. Li, *J. Cleaner Prod.*, 2015, **103**, 724–736.

4 M. Kalkuhl, O. Edenhofer and K. Lessman, *Environ. Resour. Econ.*, 2015, **60**, 55–80.

5 A. A. Lacis, G. A. Schmidt, D. Rind and R. A. Ruedy, *Science*, 2010, **330**, 356–359.

6 P. Fiedlinstein, R. M. Andrew, J. Rogelj, G. P. Peters, J. G. Canadell, R. Knutti, G. Luderer, M. R. Raupach, M. Schaeffer, D. P. van Vuuren and C. Le Quéré, *Nat. Geosci.*, 2014, **7**, 709–715.

7 *Climate Change 2013: The Physical Science Basis, Contribution of Working Group I to the Fifth Assessment Report of the Intergovernmental Panel on Climate Change*, ed. T. F. Stocker, D. Qin, G. K. Plattner, M. M. B. Tignor, S. K. Allen, J. Boschung, A. Nauels, Y. Xia, V. Bex and P. M. Midgley, Cambridge Univ. Press, New York, USA, 2013.

8 R. L. Revesz, P. H. Hpward, K. Arrow, L. H. Goulder, R. E. Kopp, M. A. Livermore, M. Oppenheimer and T. Sterner, *Nature*, 2014, **508**, 173–175.

9 R. S. J. Tol, *Clim. Change*, 2013, **117**, 795–808.

10 R. J. Andres, T. A. Boden, F. N. Bréon, P. Ciais, S. Davis, D. Erickson, J. S. Gregg, A. Jacobson, G. Marland, J. T. Miller, T. Oda, J. G. J. Olivier, M. R. Raupach, P. Rayner and K. Treanton, *Biogeosciences*, 2012, **9**, 1845–1871.

11 M. Höök and X. Tang, A Review, *Energy Policy*, 2013, **52**, 797–809.

12 N. Muradov, *Liberating Energy from Carbon: Introduction to Decarbonization*, Springer, New York, 2014.

13 S. J. Davis, K. Cladeira and H. D. Matthews, *Science*, 2010, **329**, 1330–1333.

14 CO_2 Emissions from Fuel Combustion-2013, International Energy Agency, 2013.

15 Annual Energy Outlook 2014, U.S. Energy Information Administration, Washington, US, 2014.

16 World Energy Outlook 2013, International Energy Agency, 2013.

17 C. W. Jones, *Annu. Rev. Chem. Biomol. Eng.*, 2011, **2**, 31–52.

18 G. Luderer, V. Bosetti, M. Jakob, M. Leimbach, J. C. Steckel, H. Waisman and O. Edenhofer, *Clim. Change*, 2012, **114**, 9–37.

19 S. J. Friedman, CO_2 Capture and sequestration, in *Fossil Energy*, ed. R. Malhotra, Springer, Menlo Park, CA, USA, 2013, ch. 16.

20 S. D. Kenarsari, D. Yang, G. Jiang, S. Zhang, J. Wang, A. G. Russell, Q. Wei and M. Fan, *RSC Adv.*, 2013, **3**, 22739–22773.

21 M. E. Boot-Handford, J. C. Abanades, E. J. Anthony, M. J. Blunt, S. Brandani, N. Mac Dowell, J. R. Fernández, M. C. Ferrari, R. Gross, J. P. Hallett, R. S. Haszeldine, P. Heptonstal, A. Lyngfelt, Z. Makuch, E. Mangano, R. T. J. Porter, M. Pourkashanian, G. T. Rochelle, N. Shah, J. G. Yao and P. S. Fennell, *Energy Environ. Sci.*, 2014, **7**, 130–189.

22 D. Y. C. Leung, G. Caramanna and M. M. Maroto-Valer, *Renewable Sustainable Energy Rev.*, 2014, **39**, 426–443.

23 L. Raynal, P. A. Bouillon, A. Gomez and P. Broutin, *Chem. Eng. J.*, 2011, **171**, 742–752.

24 P. Markewitz, W. Kuckshinrichs, W. Leitner, J. Linssen, P. Zapp, R. Bongartz, A. Schreiber and T. E. Müller, *Energy Environ. Sci.*, 2012, **5**, 7281–7305.

25 V. Scott, S. Gilfillan, N. Markusson, H. Chalmers and R. S. Haszeldine, *Nat. Clim. Change*, 2013, **3**, 105–111.

26 G. T. Rochelle, *Science*, 2009, **325**, 1652–1654.

27 H. Lepaumier, D. Picq and P. L. Carrette, *Ind. Eng. Chem. Res.*, 2009, **48**, 9061–9067.

28 S. Chi and G. T. Rochelle, *Ind. Eng. Chem. Res.*, 2002, **41**, 4178–4186.

29 J. Kittel, R. Idem, D. Gelowitz, P. Tontiwachwuthikul, G. Parrain and A. Bonneau, *Energy Procedia*, 2009, **1**, 791–797.

30 M. R. M. Abu-Zahra, J. P. M. Niederer, P. H. M. Feron and G. F. Versteeg, *Int. J. Greenhouse Gas Control*, 2007, **1**, 135–142.

31 L. M. Romeo, I. Bolea and J. M. Escosa, *Appl. Therm. Eng.*, 2008, **28**, 1039–1046.

32 A. B. Rao and E. S. Rubin, *Environ. Sci. Technol.*, 2002, **36**, 4467–4475.

33 A. B. Rao and E. S. Rubin, *Ind. Eng. Chem. Res.*, 2006, **45**, 2421–2429.

34 A. S. Bhown and B. C. Freeman, *Environ. Sci. Technol.*, 2011, **45**, 8624–8632.

35 J. Husebye, A. L. Brunsvold, S. Roussanaly and X. Zhang, *Energy Procedia*, 2012, **23**, 381–390.

36 K. Sumida, D. L. Rogow, J. A. Mason, T. M. McDonald, E. D. Bloch, Z. R. Herm, T. H. Bae and J. R. Long, *Chem. Rev.*, 2012, **112**, 724–781.

37 A. Samantha, A. Zhao, G. K. H. Shimizu, P. Sarkar and R. Gupta, *Ind. Eng. Chem. Res.*, 2012, **51**, 1438–1463.

38 M. D. Hornboster, J. Bao, G. Krishnan, A. Nagar, I. Jayaweera, T. Kobayashi, A. Sanjurjo, J. Sweeney, D. Carruthers, M. A. Petruska and L. Dubois, *Carbon*, 2013, **56**, 77–85.

39 M. Pera-Titus, *Chem. Rev.*, 2014, **114**, 1413–1492.

40 F. Karadas, M. Atilhan and S. Aparicio, *Energy Fuels*, 2010, **24**, 5817–5828.

41 X. Zhang, X. Zhang, H. Dong, Z. Zhao, S. Zhang and Y. Huang, *Energy Environ. Sci.*, 2012, **5**, 6668–6681.

42 M. Ramdin, T. W. de Loos and T. J. H. Vlugt, *Ind. Eng. Chem. Res.*, 2012, **51**, 8149–8177.

43 R. Biczak, B. Pawlowska and P. Balczewski, *J. Hazard. Mater.*, 2014, **274**, 181–190.

44 T. P. N. Pham, C. W. Cho and Y. S. Yun, *Water Res.*, 2010, **44**, 352–372.

45 B. Peric, J. Sierra, E. Martí, R. Cruañas, M. A. Garau, J. Arning, U. Bottin-Weber and S. Stolte, *J. Hazard. Mater.*, 2013, **261**, 99–105.

46 M. Smiglak, W. M. Reichert, J. D. Holbrey, J. S. Wilkes, L. Sun, J. S. Thrasher, K. Kirichenko, S. Singh, A. R. Katritzky and R. D. Rogers, *Chem. Commun.*, 2006, 2554–2556.

47 K. Paduszynski and U. Dománska, *J. Chem. Inf. Model.*, 2014, **54**, 1311–1324.

48 L. Chen, M. Sharifzadeh, N. MacDowell, T. Welton, N. Shah and J. P. Hallett, *Green Chem.*, 2014, **16**, 3098–3106.

49 M. Petkovic, K. R. Seddon, L. P. N. Rebelo and C. Silva-Pereira, *Chem. Soc. Rev.*, 2011, **40**, 1383–1403.

50 S. P. M. Ventura, F. Silva, A. M. M. Goncalves, J. L. Pereira, F. Goncalves and J. A. P. Coutinho, *Ecotoxicol. Environ. Saf.*, 2014, **102**, 48–54.

51 X. D. Hou, Q. P. Liu, T. J. Smith, N. Li and M. H. Zong, *PLoS One*, 2013, **8**, e59145.

52 C. Asumana, G. Yu, X. Li, J. Zhao, G. Liu and X. Chen, *Green Chem.*, 2010, **12**, 2030–2037.

53 A. Paiva, R. Caraverio, I. Aroso, M. Martins, R. L. Reis and A. R. C. Duarte, *ACS Sustainable Chem. Eng.*, 2014, **2**, 1063–1071.

54 Q. Zhang, K. O. Vigier, S. Royer and F. Jérôme, *Chem. Soc. Rev.*, 2012, **41**, 7108–7146.

55 H. G. Morrison, C. C. Sun and S. Neervannan, *Int. J. Pharm.*, 2009, **378**, 136–139.

56 B. S. Singh, H. R. Lobo and G. S. Shankarling, *Catal. Commun.*, 2012, **24**, 70–74.

57 Y. H. Choi, J. van Spronsen, Y. T. Dai, M. Vermerne, F. Hollmann, I. W. C. E. Arends, G. J. Witkamp and R. Verpoorte, *Plant Physiol.*, 2011, **156**, 1701–1705.

58 Y. Dai, J. van Spronsen, G. J. Witkamp, R. Verpoorte and Y. H. Choi, *Anal. Chim. Acta*, 2013, **766**, 61–68.

59 Z. Maugeri and P. Domínguez, *RSC Adv.*, 2012, **2**, 421–425.

60 C. Florindo, F. S. Oliveira, L. P. N. Rebelo, A. M. Fernandes and I. M. Marrucho, *ACS Sustainable Chem. Eng.*, 2014, **2**, 2416–2425.

61 J. Bozell, L. Moens, D. C. Elliott, Y. Wang, G. G. Neuenscwander, S. W. Fitzpatrick, R. J. Bilski and J. L. Jarnefeld, *Resour., Conserv. Recycl.*, 2000, **28**, 227–239.

62 C. Chang, P. Cen and X. Ma, *Bioresour. Technol.*, 2007, **98**, 1448–1453.

63 R. Weingartner, W. C. Conner and G. W. Huber, *Energy Environ. Sci.*, 2012, **5**, 7559–7574.

64 X. Li, M. Hou, B. Han, X. Wang and L. Zou, *J. Chem. Eng. Data*, 2008, **53**, 548–550.

65 R. B. Leron, A. Caparanga and M. L. Li, *J. Taiwan Inst. Chem. Eng.*, 2013, **44**, 879–885.

66 R. B. Leron and M. H. Li, *Thermochim. Acta*, 2013, **551**, 14–19.

67 R. B. Leron and M. H. Li, *J. Chem. Thermodyn.*, 2013, **57**, 131–136.

68 M. Francisco, A. van den Bruinhorst, L. F. Zubeir, C. J. Peters and M. C. Kroon, *Fluid Phase Equilib.*, 2013, **340**, 77–84.

69 Y. C. Chen, N. Ai, H. Shan, Y. Cui and D. Deng, *J. Chem. Eng. Data*, 2014, **59**, 1247–1253.

70 C.-M. Lin, R. B. Leron, A. R. Caparanga and M. H. Li, *J. Chem. Thermodyn.*, 2014, **68**, 216–220.

71 Y. Chen, N. Ai, H. Shan, Y. Cui and D. Deng, *J. Chem. Eng. Data*, 2014, **59**, 1247–1253.

72 G. Li, D. Deng, Y. Chen, H. Shan and N. Ai, *J. Chem. Thermodyn.*, 2014, **75**, 58–62.

73 P. Hapiot and C. Lagrost, *Chem. Rev.*, 2008, **108**, 2238–2264.

74 A. P. Abbott, D. Boothby, G. Capper, D. L. Davies and R. K. Rasheed, *J. Am. Chem. Soc.*, 2004, **126**, 9142–9147.

75 ASTM Standard G1-03, Standard Practice for Preparing, Cleaning and Evaluating Corrosion Test Specimens, Annual Book of ASTM Standards American Society of Testing Materials, West Conshohcken, PA, 2003.

76 F. Karadas, C. T. Yavuz, S. Zulfiqar, S. Aparicio, G. D. Stucky and M. Atilhan, *Langmuir*, 2011, **27**, 10642–10647.

77 D. E. Cristancho, I. D. Mantilla, S. Ejaz, K. R. Hall, G. A. Iglesias-Silva and M. Atilhan, *Int. J. Thermophys.*, 2009, **31**, 698–709.

78 C. Lee, W. Yang and R. G. Parr, *Phys. Rev. B: Condens. Matter Mater. Phys.*, 1988, **37**, 785–789; A. D. Becke, *J. Chem. Phys.*, 1993, **98**, 5648–5652.

79 A. D. Becke, *Phys. Rev. A: At., Mol., Opt. Phys.*, 1988, **38**, 3098–3100.

80 S. Grimme, *J. Comput. Chem.*, 2006, **27**, 1787–1799.

81 A. J. Cohen, P. Mori-Sánchez and W. Yang, *Chem. Rev.*, 2012, **112**, 289–320.

82 T. Schwabe and S. Grimme, *Phys. Chem. Chem. Phys.*, 2007, **9**, 3397–3406.

83 S. Simon, M. Duran and J. J. Dannenberg, *J. Chem. Phys.*, 1996, **105**, 11024.

84 R. F. W. Bader, *Atoms in Molecules: a Quantum Theory*, Oxford, 1990.

85 T. Lu and F. J. Chen, *J. Comput. Chem.*, 2012, **33**, 580–592.

86 C. M. Breneman and K. B. Wiberg, *J. Comput. Chem.*, 1990, **11**, 361–373.

87 M. J. Frisch, G. W. Trucks, H. B. Schlegel, G. E. Scuseria, M. A. Robb, J. R. Cheeseman, G. Scalmani, V. Barone, B. Mennucci, G. A. Petersson, H. Nakatsuji, M. Caricato, X. Li, H. P. Hratchian, A. F. Izmaylov, J. Bloino, G. Zheng, J. L. Sonnenberg, M. Hada, M. Ehara, K. Toyota, R. Fukuda, J. Hasegawa, M. Ishida, T. Nakajima, Y. Honda, O. Kitao, H. Nakai, T. Vreven, J. A. Montgomery, Jr., J. E. Peralta, F. Ogliaro, M. Bearpark, J. J. Heyd, E. Brothers, K. N. Kudin, V. N. Staroverov, R. Kobayashi, J. Normand, K. Raghavachari, A. Rendell, J. C. Burant, S. S. Iyengar, J. Tomasi, M. Cossi, N. Rega, J. M. Millam, M. Klene, J. E. Knox, J. B. Cross, V. Bakken, C. Adamo, J. Jaramillo, R. Gomperts, R. E. Stratmann, O. Yazyev, A. J. Austin, R. Cammi, C. Pomelli, J. W. Ochterski, R. L. Martin, K. Morokuma, V. G. Zakrzewski, G. A. Voth, P. Salvador, J. J. Dannenberg, S. Dapprich, A. D. Daniels, Ö. Farkas, J. B. Foresman, J. V. Ortiz, J. Cioslowski and D. J. Fox, *Gaussian 09, Revision D.01*, Gaussian, Inc., Wallingford, CT, USA, 2009.

88 L. Martínez, R. Andrade, E. G. Birgin and J. M. Martínez, *J. Comput. Chem.*, 2009, **30**, 2157–2164.

89 E. W. Lemmon, M. L. Huber and M. O. McLinden, *NIST Standard Reference Database 23: Reference Fluid Thermodynamic and Transport Properties-REFPROP, Version 9.1*, National Institute of Standards and Technology, Standard Reference Data Program, Gaithersburg, 2013.

90 A. P. Lyubartsev and A. Laaksonen, *Comput. Phys. Commun.*, 2000, **128**, 565–589.

91 U. L. Essmann, M. L. Perera, T. Berkowitz, H. Darden, H. Lee and L. G. Pedersen, *J. Chem. Phys.*, 1995, **103**, 8577–8593.

92 M. Tuckerman, B. J. Berne and G. J. Martyna, *J. Chem. Phys.*, 1992, **97**, 1990–2001.

93 W. Guo, Y. Hou, S. Ren, S. Tian and W. Wu, *J. Chem. Eng. Data*, 2013, **58**, 866–872.

94 C. D'Agostino, R. C. Harris, A. P. Abbott, L. F. Gladden and M. D. Mantle, *Phys. Chem. Chem. Phys.*, 2011, **13**, 21383–21391.

95 A. Yadav, S. Trivedi, R. Rai and S. Pandey, *Fluid Phase Equilib.*, 2014, **367**, 135–142.

96 G. García, S. Aparicio, R. Ullah and M. Atilhan, *Energy Fuels*, 2015, **29**, 2616–2644.

97 A. Abbott, E. I. Ahmed, R. C. Harris and K. S. Ryder, *Green Chem.*, 2014, **16**, 4156–4161.

98 E. W. Lemmon, M. L. Huber and M. O. McLinden, *NIST Reference Fluid Thermodynamic and Transport Properties REFPROP, Version 8.0*, National Institute of Standards and Technology, Standard Reference Data Program, Gaithersburg, MD, 2007.

99 S. L. Perkins, P. Painter and C. M. Colina, *J. Phys. Chem. B*, 2013, **117**, 10250–10260.

100 S. P. Verevkin, D. H. Zaitsau, V. N. Emel'yanenko, A. V. Yermalayeu, C. Schick, H. Liu, E. J. Maginn, S. Bulut, I. Krossing and R. Kalb, *J. Phys. Chem. B*, 2013, **117**, 6473–6486.

101 Y. Zhang and E. J. Maginn, *Phys. Chem. Chem. Phys.*, 2014, **16**, 13489–13499.

102 H. Sun, Y. Li and G. Li, *J. Mol. Model.*, 2013, **19**, 2433–2441.

103 G. García, J. L. Trenzado, R. Alcalde, A. Rodriguez-Delgado, M. Atilhan and S. Aparicio, *J. Phys. Chem. B*, 2014, **118**, 11310–11322.